Wnt/PCP signaling mediates breast cancer metastasis by promoting pro-invasive protrusion formation in collectively motile leader cells

Kacey VanderVorst[1], Courtney A. Dreyer[1], Jason Hatakeyama[2], George R. R. Bell[3], Anastasia L. Berg[1], Maria Hernandez[1], Hyun Lee[1], Sean R. Collins[3] and Kermit L. Carraway III[1]*

[1]Department of Biochemistry and Molecular Medicine and University of California Davis Comprehensive Cancer Center, University of California Davis School of Medicine, Sacramento, CA, USA

[2]Institute for Stem Cell Biology and Regenerative Medicine, Stanford University School of Medicine, Stanford, CA, USA

[3]Department of Microbiology and Molecular Genetics, University of California Davis, Davis, CA, USA

*To whom correspondence should be addressed: klcarraway@ucdavis.edu

Abstract

As evidence supporting essential roles for collective cell migration in carcinoma metastasis continues to accumulate, a better understanding of the underlying cellular and molecular mechanisms will be critical to translating these findings to the treatment of advanced cancers. Here we report that Wnt/PCP, a non-canonical Wnt signaling pathway, mediates breast cancer collective migration and metastasis. We observe that mammary gland-specific knockout of *Vangl2*, a tetraspanin-like scaffolding protein required for Wnt5a-induced signaling and motility in cultured breast cancer cell lines, results in a striking decrease in metastatic efficiency but not primary tumor growth in the *MMTV-NDL* transgenic mouse model of HER2-positive breast cancer. We also observe that expression levels of core Wnt/PCP components *Wnt5a*, *Vangl1* and *Vangl2* are selectively elevated in K14-positive leader cells relative to follower cells within a collectively migrating cohort, and that *Vangl2* expression selectively promotes RhoA activation in leading edge cells. Moreover, *Vangl* expression drives collective migration in three-dimensional *ex vivo* tumor organoids, and Vangl protein specifically accumulates within pro-migratory filamentous actin-rich protrusions of leader cells. Together, our observations point to a model whereby Wnt/PCP upregulation facilitates breast tumor collective cell motility by selectively augmenting the formation pro-migratory protrusions within leader cells.

Introduction

Metastasis is a complex, multi-step process whereby cancer cells invade into surrounding tissues, access and traverse the vasculature, disseminate throughout the body, and proliferate at secondary sites (Talmadge & Fidler, 2010). Observations that carcinoma cells invade almost exclusively in a collective manner (Bronsert et al., 2014), and that metastatic lesions may be largely seeded by polyclonal cell clusters rather than individual disseminated cells (Aceto et al., 2014; Cheung et al., 2016; Fischer et al., 2015; Hou et al., 2012), strongly suggest that collective cell migration, defined as the coordinated movement of cohorts of cells in sheets or clusters that retain cell-cell contacts (Friedl & Gilmour, 2009), is a major driver of invasiveness and metastasis. In non-transformed tissues, collective cell migration promotes blood vessel formation (Geudens & Gerhardt, 2011), convergent extension (Davey & Moens, 2017), branching morphogenesis (Ewald et al., 2008), and wound healing (Friedl & Gilmour, 2009). However, the study of collective cell migration in carcinomas significantly lags that of classical epithelial-mesenchymal transition (EMT)-mediated motility of individual cells. Thus, a better understanding of cell signaling pathways that govern collective cell migration and invasiveness may identify novel therapeutic targets to intervene in patients with aggressive and late-stage disease.

We recently proposed a model whereby aberrant activation of Wnt/planar cell polarity (Wnt/PCP) signaling (VanderVorst et al., 2019), a branch of non-canonical Wnt signaling paradoxically critical to both the establishment and maintenance of polarity in epithelial sheets as well as cell migration during embryonic development (Butler & Wallingford, 2017; Caddy et al., 2010), promotes the invasiveness of primary tumor cells. In Wnt/PCP signaling, binding of non-canonical Wnt ligands such as Wnt5a to transmembrane Frizzled (Fzd) receptors initiates polarization signals that are transduced through the essential pathway components Vangl, Dishevelled (Dvl), and Prickle (Pk) (Chu & Sokol, 2016; Minegishi et al., 2017; Wu et al., 2013). Although Dvl and Fzd are required for both canonical and alternative non-canonical Wnt pathways, the unique engagement of Vangl1

and Vangl2 transmembrane scaffolds in Wnt/PCP signaling may provide the platform necessary for the assembly of pathway-specific complexes (VanderVorst et al., 2018). Vangl1 and Vangl2 are highly similar; their amino acid sequences exhibit 64.3% identity and 78.6% similarity, and no functional biochemical differences have been reported (Hatakeyama et al., 2014). However, Vangl2 alterations result in more profound developmental defects, suggesting a more prominent role for Vangl2 in embryonic tissue organization (Belotti et al., 2012; Hatakeyama et al., 2014). Wnt/PCP signaling is a significant driver of collective cell migration in development (Carmona-Fontaine et al., 2008; Ybot-Gonzalez et al., 2007), and studies employing Looptail (Lp) mice, which harbor point mutations in Vangl2 that alter its trafficking and localization, suggest that Vangl subcellular localization is critical in collectively migrating cells (Murdoch et al., 2001).

Consistent with observations from developmental studies, Wnt/PCP components mediate cell motility in cancer cells (Asad et al., 2014; Kurayoshi et al., 2006), and core Wnt/PCP components are dysregulated in multiple tumor types, including breast (Anastas et al., 2012; Daulat et al., 2016; Luga et al., 2012; MacMillan et al., 2014; Pukrop et al., 2006; Puvirajesinghe et al., 2016; Zhang et al., 2016), brain (Wald et al., 2017), ovarian (Asad et al., 2014), prostate (Uysal-Onganer et al., 2010), gastric (Kurayoshi et al., 2006), and colorectal cancers (Nishioka et al., 2013; Ueno et al., 2008). We have reported that *VANGL1* and *VANGL2* are respectively upregulated in 5% and 24% of invasive breast carcinomas compared to healthy breast tissue (Hatakeyama et al., 2014), and others have found that elevated *VANGL1* and *VANGL2* are also associated with increased recurrence and decreased metastasis-free survival of breast cancer patients (Anastas et al., 2012; Puvirajesinghe et al., 2016). Together, these observations point to the possibility that aberrant Wnt/PCP activation contributes to breast cancer progression by promoting collective cell migration resulting in metastasis.

Here we examine the role of Vangl-dependent Wnt/PCP signaling in breast cancer invasiveness and metastasis. We demonstrate that Vangl2 is critical for efficient metastasis but dispensable for primary tumor growth in ErbB2-induced mouse mammary tumors. We further find that Vangl-dependent Wnt/PCP signaling at the leading edge of migrating breast cancer cells results in increased RhoA GTPase activity and formation of pro-migratory protrusions, resulting in collective cell migration *in vitro* and invasion *ex vivo*.

Results

Vangl2 deletion suppresses mammary tumor metastasis to the lungs but does not alter primary tumor growth

We assessed the functional importance of Vangl2 to mammary tumorigenesis and tumor cell metastatic dissemination by specifically ablating *Vangl2* in the mammary epithelium of *MMTV-NDL* mice. In this well-characterized genetically engineered mouse model of breast cancer, an activated ErbB2 mutant encoded by the transgenic rat *c-ErbB2/neu* allele under the control of the MMTV promoter drives the formation of metastatic multifocal mammary tumors at approximately 20 weeks of age (Siegel et al., 1999) (Figure 1A). Effective deletion of *Vangl2* in mammary tumors of *Vangl2*$^{fl/fl}$*;MMTV-Cre*$^{+/-}$*;MMTV-NDL*$^{+/-}$ (Vangl2$^{fl/fl}$/NDL) mice relative to *Vangl2*$^{fl/fl}$*;MMTV-NDL*$^{+/-}$ (Vangl2$^{+/+}$/NDL) mice was confirmed by *q*PCR (Figure 1–figure supplement 1A). Although *Vangl1* may compensate for loss of *Vangl2* in some contexts (Hatakeyama et al., 2014), *Vangl1* transcript is not significantly altered in Vangl2$^{fl/fl}$/NDL mammary tumors relative to Vangl2$^{+/+}$/NDL tumors (Figure 1–figure supplement 1B). *Vangl2* ablation did not produce discernable effects on viability, breeding, or lactation, and no differences in mammary gland architecture were noted between genotypes in adult virgin mammary glands (Figure 1–figure supplement 1C).

Despite similar kinetics of primary tumor initiation and growth in Vangl2$^{+/+}$/NDL and Vangl2$^{fl/fl}$/NDL mice (Figure 1–figure supplement 2A-D), *Vangl2*-depleted tumors are significantly less metastatic than *Vangl2*-intact tumors (Figure 1B-E). Analysis of lung tissue revealed that deletion of *Vangl2* in *MMTV-NDL* tumors results in significantly reduced frequency of metastatic disease (Figure 1C), number of lung metastases (Figure 1D) and overall metastatic burden (Figure 1E) despite similar primary tumor characteristics such as numbers of palpable tumors (Figure 1F), total tumor volume (Figure 1G), average tumor volume (Figure 1H), tissue histology (Figure 1–figure supplement 2E,F), proliferative capacity (Figure 1–figure supplement 2G,H), and apoptosis (Figure 1–figure

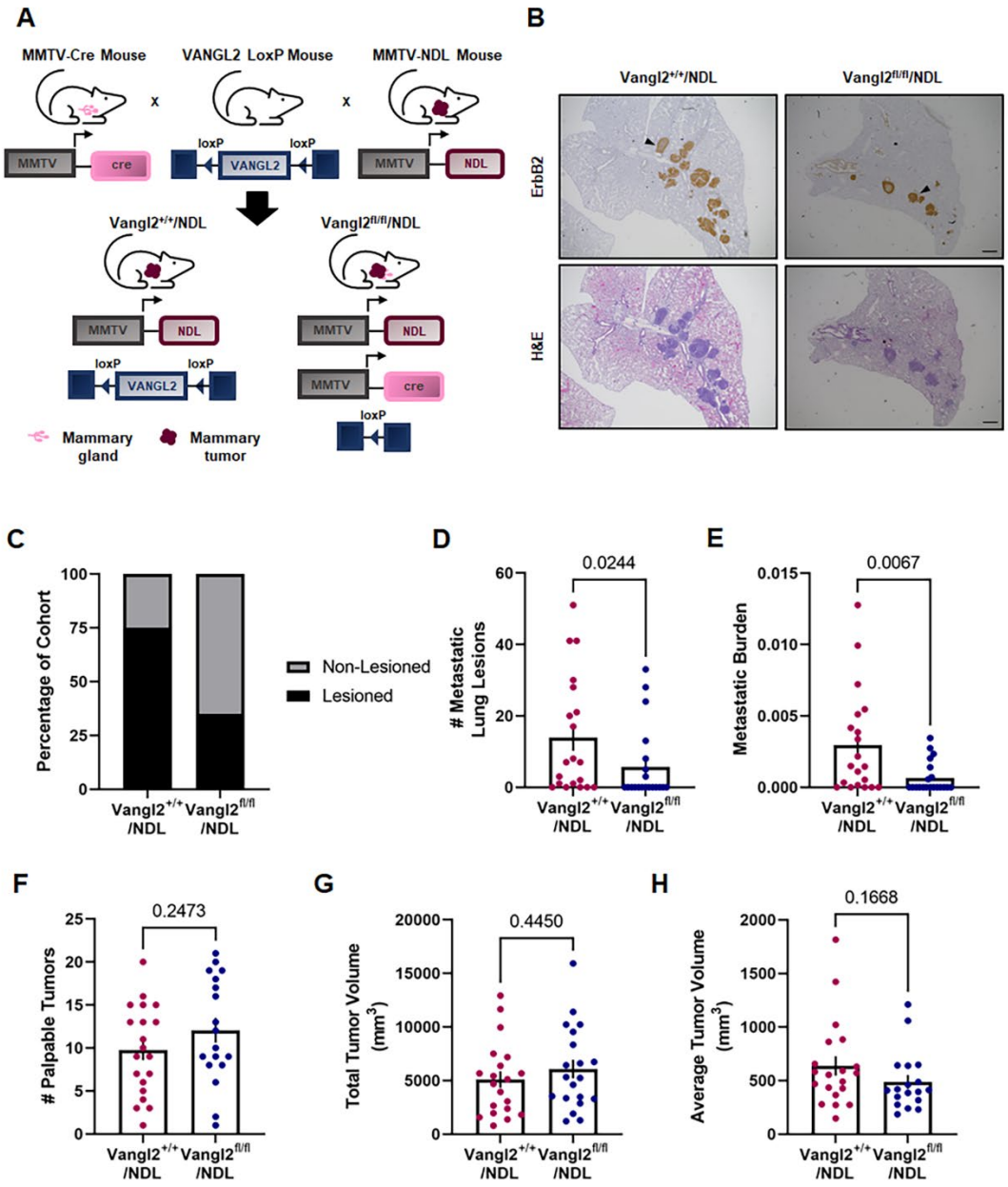

Figure 1. Vangl2 deletion suppresses mammary tumor metastasis to the lung. A Summary of the transgenic mouse strategy employed to assess Vangl2 deletion in mammary tumorigenesis. **B** Representative images of formalin fixed, paraffin embedded sections from Vangl2$^{+/+}$/NDL and Vangl2$^{fl/fl}$/NDL lung tissue following immunodetection of ErbB2 (top panel) and H&E staining (bottom panel). Examples of ErbB2-positive metastatic lung lesions are denoted by black arrowheads, scale bar =500μm. **C-E** Lung lobes (5 lobes per mouse) were evaluated by histology for the occurrence of metastatic lesions for Vangl2$^{+/+}$/NDL (*n*=20) and Vangl2$^{fl/fl}$/NDL tumor-bearing mice (*n*=20). The number of mice bearing metastatic lesions **(C)**, numbers of metastatic lesions **(D)**, and metastatic burden **(E)** were assessed. **F-H** Vangl2/NDL primary tumor growth characteristics were assessed for Vangl2$^{+/+}$/NDL (*n*=20) and Vangl2$^{fl/fl}$/NDL (*n*=20) tumor-bearing animals, including number of palpable tumors **(F)**, total tumor volume **(G)**, and average tumor volume **(H)**. Significance was determined by Mann-Whitney test and bar graphs represent the mean ± sem of experimental replicates (*n*).

supplement 2I,J). Importantly, *Vangl2* appears to be critical to successful metastatic colonization of the lungs (Figure 1D,E) but is not required for proliferation of metastatic lesions in Vangl2$^{+/+}$/NDL and Vangl2$^{fl/fl}$/NDL mice (Figure 1–figure supplement 3A,B). Further, cells derived from Vangl2$^{+/+}$/NDL and Vangl2$^{fl/fl}$/NDL tumors injected into the tail veins of FvB/NJ mice exhibit no differences in metastatic lesion colonization efficiency (Figure 1–figure supplement 3C-F). Taken together, these findings suggest that the reduced incidence of metastasis observed upon *Vangl2* ablation is the result of reduced dissemination from the primary tumor rather than suppressed outgrowth of colonies in the lungs. Because Wnt/PCP signaling is vital to collective cell motility events critical to embryonic tissue patterning (Butler & Wallingford, 2017; Hatakeyama et al., 2014), we hypothesized that Vangl2 facilitates local invasion and migration from the primary tumor, resulting in dissemination and metastatic disease.

Vangl2-dependent Wnt/PCP signaling promotes breast cancer cell migration

We interrogated whether loss of Vangl2 impacts breast cancer cell motility by employing a panel of human breast cancer cell lines encompassing several molecular subtypes: triple-negative BT549, HCC1937, HCC38, MDA-MB-157, MDA-MB-231 and MDA-MB-468, and ER/PR-positive MCF7. Cells were transduced with lentivirus encoding *VANGL2*-targeted shRNAs and knockdown was confimed by *q*PCR (Figure 2–figure supplement 1A). Loss of *VANGL2* expression significantly impairs breast cancer cell migration, indicated by the reduced ability of *VANGL2* knockdown cells to migrate into a scratch made in the cellular monolayer (Figure 2A), but does not siginificantly impair cell proliferation after 12 hours (Figure 2–figure supplement 1B). These data demonstrate that Vangl2 is critical to breast cancer cell motility, regardless of breast cancer subtype.

In motile cells, activation of Vangl-dependent Wnt/PCP signaling occurs by binding of a non-canonical Wnt ligand such as Wnt5a to Fzd receptors at the plasma membrane, resulting in

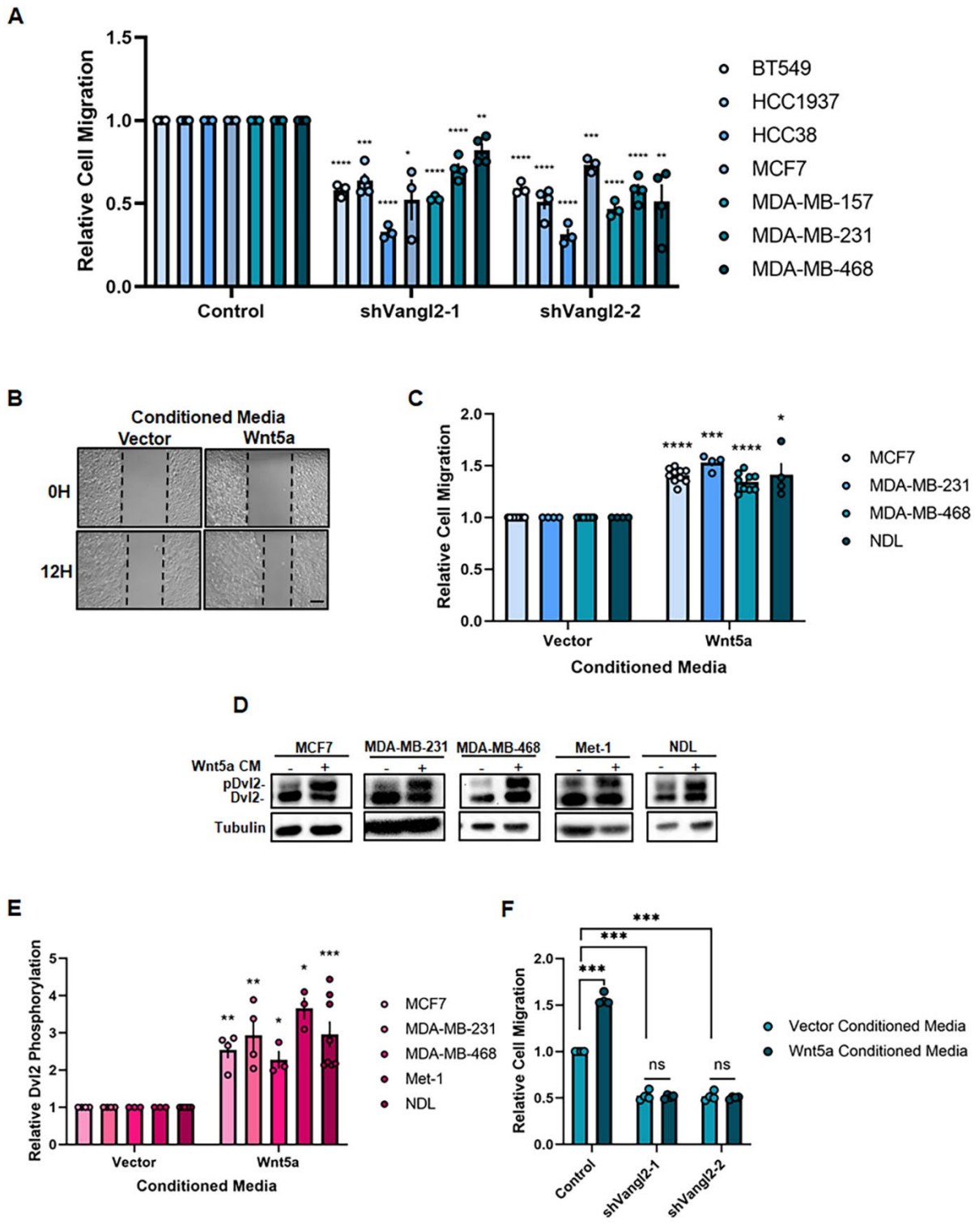

159

Figure 2. Vangl2 is essential for Wnt5a-induced Wnt/PCP signaling and breast cancer cell motility. A Relative cell migration quantification of BT549, HCC1937, HCC38, MCF7, MDA-MB-157, MDA-MB-231, and MDA-MB-468 cells stably expressing Control, shVangl2-1, or shVangl2-2 (BT549 n=3, p=4.81E-05 and p=4.47E-05, HCC1937 n=4, p=0.0002 and p=3.37E-05, HCC38 n=3, p=7.69E-06 and p=4.31E-05, MCF7 n=3, p=0.0180 and p=0.0004, MDA-MB-231 n=4, p=0.0001 and p=2.73E-05, MDA-MB-468 n=4, p=0.0046 and p=0.0033). **B** Representative images of migrating NDL cells stimulated with Vector- or Wnt5a- conditioned media at 0 and 12 hours. Scale bar = 200μm. **C** Relative cell migration quantification of MCF7, MDA-MB-231, MDA-MB-468, and NDL cells stimulated with Vector- or Wnt5a-conditioned media (MCF7 n=10, p=1.54E-08, MDA-MB-231 n=4, p=0.0006, MDA-MB-468 n=9, p=2.33E-06, NDL n=4, p=0.0344,). **D,E** MCF7, MDA-MB-231, MDA-MB-468, Met-1, and NDL cells stimulated with Vector- or Wnt5a-conditioned media for 1 hour blotted for Dvl2 **(D)** and quantification of relative Dvl2 phosphorylation (MCF7 n=4, p=0.0067, MDA-MB-231 n=4, p=0.0199, MDA-MB-468 n=3, p=0.0327, Met-1 n=3, p=0.0121, NDL n=8, p=0.0007) **(E)**. **F** Relative cell migration quantification of MDA-MB-231 cells stably expressing Control, shVangl2-1, or shVangl2-2 stimulated with Vector- or Wnt5a- conditioned media (control: vector- vs Wnt5a-conditioned media n=4, p=0.0003, Control vs shVangl2-1 + vector-conditioned media n=4, p=0.0003, control vs shVangl2-2 + vector-conditioned media n=4, p= 0.0003, shVangl2-1: vector- vs Wnt5a-conditioned media n=4, p=0.7256, shVangl2-2: vector- vs Wnt5a-conditioned media n=4, p=0.5804). Bar graphs represent the mean ± sem of experimental replicates (n). Significance was determined by a two-sided unpaired t-test with Welch's correction, *p < 0.05, **p < 0.01, ***p < 0.001, ****p < 0.0001.

recruitment and phosphorylation of Dvl. Transmembrane proteins Vangl1 and Vangl2 and activated Dvl may serve as both scaffolds and activators of downstream effector components that mediate context- and tissue-specific actin cytoskeletal rearrangements to promote cellular motility (Wald et al., 2017). Consistent with previous reports (MacMillan et al., 2014), we found that Wnt5a is a potent activator of Wnt/PCP signaling that drives breast cancer cell migration. Stimulation of breast cancer cell lines with Wnt5a-conditioned media enhances cellular migration (Figure 2B,C) and robustly increases phosphorylation of Dvl2 (Figure 2D,E) compared to vector control-conditioned media. To exclude the possibility that Wnt5a activates the canonical Wnt pathway, we assessed phosphorylation of β-catenin, a marker of canonical Wnt signaling (van Amerongen, 2012). Stimulation of MCF7 cells with Wnt5a-conditioned media does not significantly impact β-catenin phosphorylation, whereas stimulation with conditioned media containing the potent canonical Wnt activating ligand Wnt3a significantly reduces β-catenin phosphorylation (Figure 2–figure supplement 1C-D). Thus, Wnt5a-dependent migration and Dvl2 phosphorylation in breast cancer cells is driven by engagement of a non-canonical rather than canonical Wnt signaling pathway.

Dvl2 phosphorylation is also a common feature of other non-canonical Wnt pathways independent of Wnt/PCP signaling (Semenov et al., 2007), and while a downstream effector specific to Wnt/PCP signaling has yet to be identified, this branch of non-canonical Wnt signaling requires the formation of Vangl-dependent complexes (Hatakeyama et al., 2014). We determined that Wnt5a-mediated migration is ablated in *VANGL2* knockdown breast cancer cells (Figure 2F), demonstrating that Wnt5a specifically activates Vangl-dependent Wnt/PCP signaling in breast cancer cells.

High Vangl expression aberrantly engages Wnt/PCP signaling and enhances breast cancer cell motilty

Our observations that Vangl2 mediates mammary tumor metastasis (Figure 1) and is required for Wnt5a-mediated cell migration (Figure 2), combined with previous reports that elevated *VANGL2* expression correlates with worsened metastasis-free survival in breast cancer patients (Puvirajesinghe et al., 2016), suggest that high Vangl expression may result in enhanced cellular migration and aberrant engagement of Wnt/PCP signaling in breast tumors. To investigate this possibility, we stably overexpressed Vangl1 or Vangl2 via lentiviral infection in human and mouse breast tumor cell lines (Figure 3–figure supplement 1A,B). Breast cancer cells overexpressing Vangl1 or Vangl2 exhibit increased motility and Dvl2 phosphorylation compared to cells transduced with control lentivirus (Figure 3A, C-F), and display a distinctive hyper-protrusive leading edge morphology (Figure 3B). These observations indicate that Vangl proteins are sufficient to aberrantly engage Wnt/PCP signaling either independent of Wnt ligand or by potentiating signaling from endogenous Wnt ligand.

To distinguish between these possibilities, we treated Vangl overexpressing breast cancer cells with the Porcupine antagonist C59, which impairs palmitoylation and subsequent secretion of Wnt ligands (Proffitt et al., 2013), to deplete endogenous Wnt5a ligand. C59 treatment resulted in ablation of Vangl-mediated Dvl2 phosphorylation (Figure 3G,H), demonstrating that aberrant Wnt/PCP signaling mediated by Vangl overexpression is Wnt ligand-dependent. Taken together, these findings suggest that activation of Wnt/PCP signaling in breast cancer cells, accomplished either by exposing cells to elevated levels of non-canonical Wnt ligand or by potentiating signals from endogenous Wnt ligands through overexpression of Vangls, enhances cellular motility and may promote metastatic dissemination of primary tumor cells.

Wnt/PCP signaling drives breast carcinoma cell collective invasion

Collective cell invasion is driven by leader cells that aggressively invade while remaining attached to follower cells, resulting in the formation of contiguous invasive strands

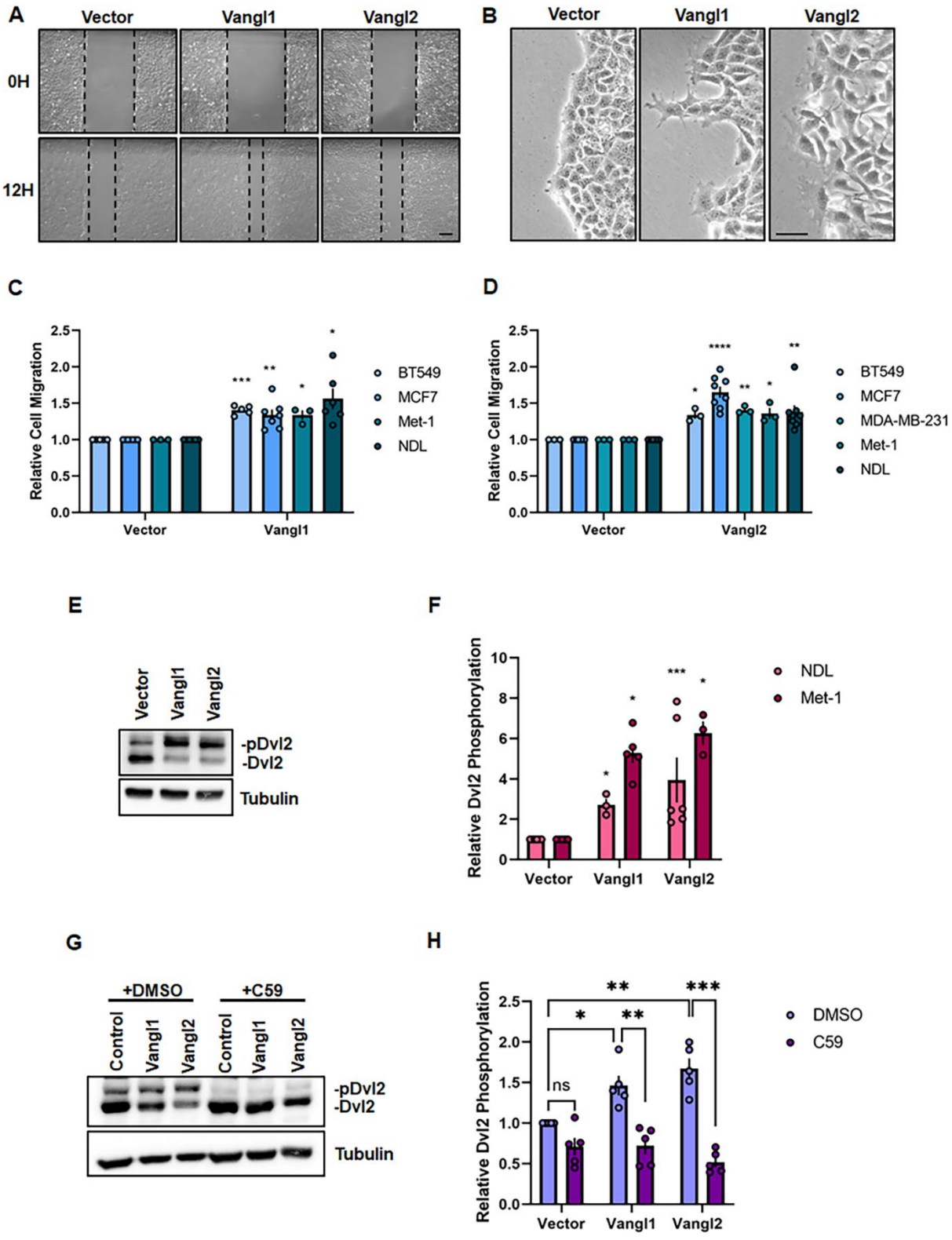

234

Figure 3. Vangl overexpression potentiates Wnt/PCP signaling and promotes breast cancer cell migration. A,B Representative brightfield images of migrating NDL cells stably expressing Vector, Vangl1, or Vangl2 at 0 and 12 hours, scale bar = 200μm **(A)** and leading-edge dynamics at 12 hours, scale bar = 50 μm **(B)**. **C** Relative cell migration quantification of BT549, MCF7**,** Met-1, and NDL cells stably expressing Vector or Vangl1 (BT549 *n*=5, *p*=0.0001, MCF7 *n*=7, *p*=0.0035, Met-1 *n*=3, *p*=0.0339, NDL *n*=6, *p*=0.0108). **D** Relative cell migration quantification of BT549, MCF7, MDA-MB-231**,** Met-1, and NDL cells stably expressing Vector or Vangl2 (BT549 *n*=3, *p*=0.0210, MCF7 *n*=8, *p*=6.17E-05, MDA-MB-231 *n*=3, *p*=0.0050, Met-1 *n*=3, *p*=0.0412, NDL *n*=8, *p*=0.0049). **E,F** NDL cells stably expressing Vector, Vangl1 or Vangl2 blotted for Dvl2 **(E)** and quantification of Dvl2 phosphorylation in NDL and Met-1 cells stably expressing Vector, Vangl1 or Vangl2 **(F)** (NDL-Vangl1 *n*=3, *p*=0.0291, NDL-Vangl2 *n*=6, *p*=0.0453, Met-1-Vangl1 *n*=5, *p*=0.0009, Met-1-Vangl1 *n*=3, *p*=0.0119). **G,H** NDL cells stably expressing Vector, Vangl1, or Vangl2 treated with DMSO or 100nM C59 for 24 hours blotted for Dvl2 **(G)** and quantification of relative Dvl2 phosphorylation **(H)**. Bar graphs represent the mean ± sem of experimental replicates (*n*). Significance was determined by a two-sided unpaired *t*-test with Welch's correction, **p* < 0.05, ***p* < 0.01, ****p* < 0.001, *****p* < 0.0001.

(Cheung et al., 2013; Cheung et al., 2016; VanderVorst et al., 2019). Invasive leader cells are molecularly and behaviorally distinct from bulk tumor cells, and in some mammary tumor models and human breast tumors express the basal epithelial marker cytokeratin 14 (K14) (Cheung et al., 2013). Importantly, K14-positive leader cells are not enriched for markers of stemness or EMT (Cheung et al., 2013), underscoring the unique character of this population and distinguishing these cells from classically defined invasive mediators of metastasis.

To investigate the contribution of Wnt/PCP signaling to breast cancer cell collective invasion, we employed an *ex vivo* 3D collagen invasion assay (Nguyen-Ngoc et al., 2012), in which tumor organoids form multicellular epithelial cell protrusions that invade a collagen matrix. Individual tumor cells derived from the highly aggressive, metastatic *MMTV-PyMT* mouse model (Guy et al., 1992; Lin et al., 2003) were first seeded in Matrigel, transduced with lentivirus encoding Wnt/PCP components (Figure 4–figure supplement 1A-C), and cultured for one week to generate tumor organoids. Organoids were then transferred to 3D collagen I gels, a model for the microenvironment surrounding invasive breast cancers (Nguyen-Ngoc et al., 2012), and a fraction of epithelial cells became K14-positive leader cells that formed multicellular protrusions of collectively invading cells upon stimulation with *b*FGF (Cheung et al., 2013).

We observed that lentiviral-mediated overexpression of Wnt5a, Vangl1, or Vangl2 significantly increases the frequency of *b*FGF-dependent collectively invading strands formed by *MMTV-PyMT* organoids (Figure 4A-C). Expression of Wnt/PCP components was not sufficient to stimulate collective invasion in the absence of *b*FGF (Figure 4–figure supplement 1D), indicating that Wnt/PCP signaling cooperates with additional signaling pathways to promote collective invasion rather than independently driving formation of invasive protrusions. Our data suggest that Vangl1 is highly expressed in K14-positive cells at the tip of invading strands compared to K14-negative follower cells or non-invading tumor organoid cells (Figure 4D), indicating that Wnt/PCP signaling

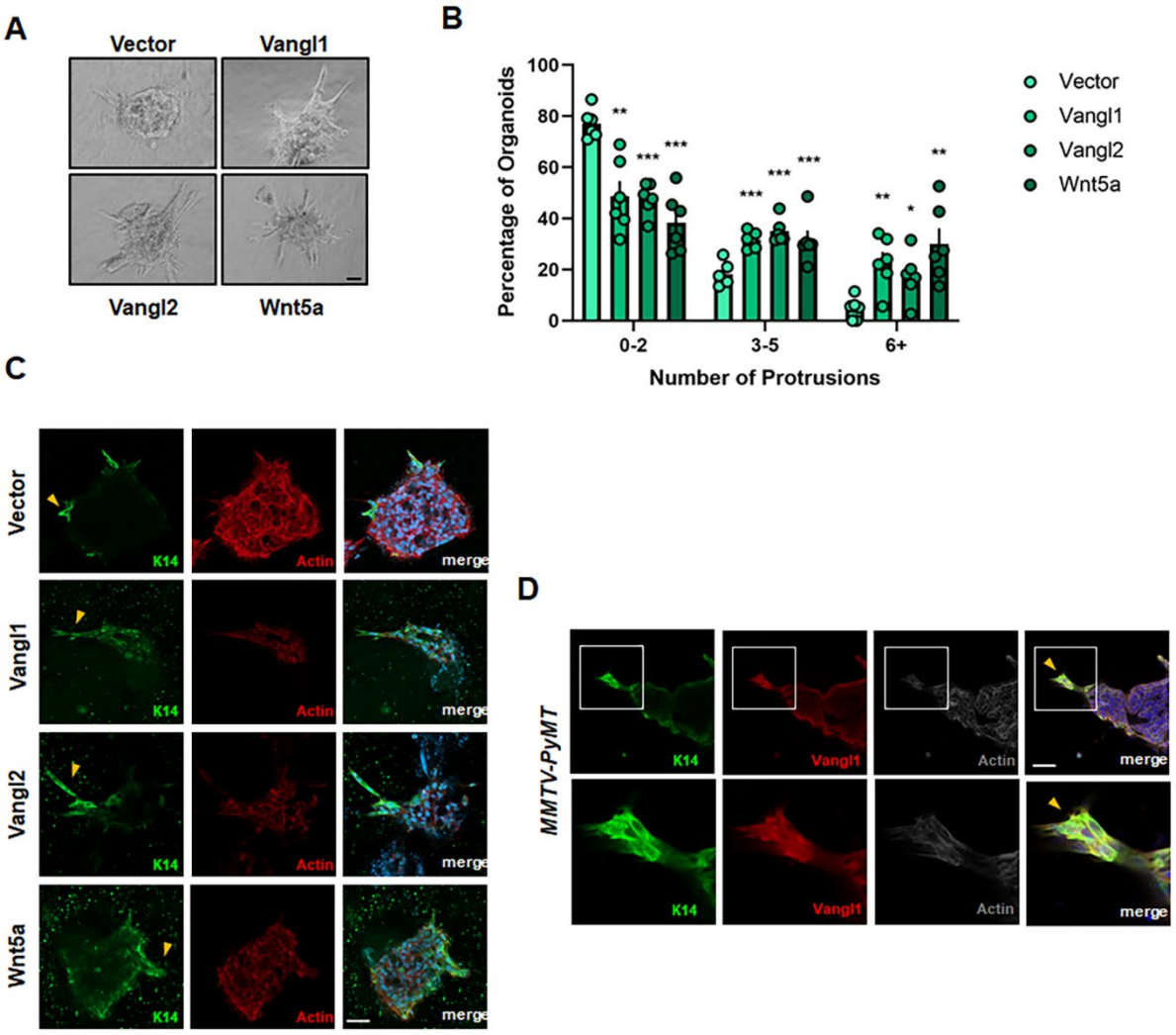

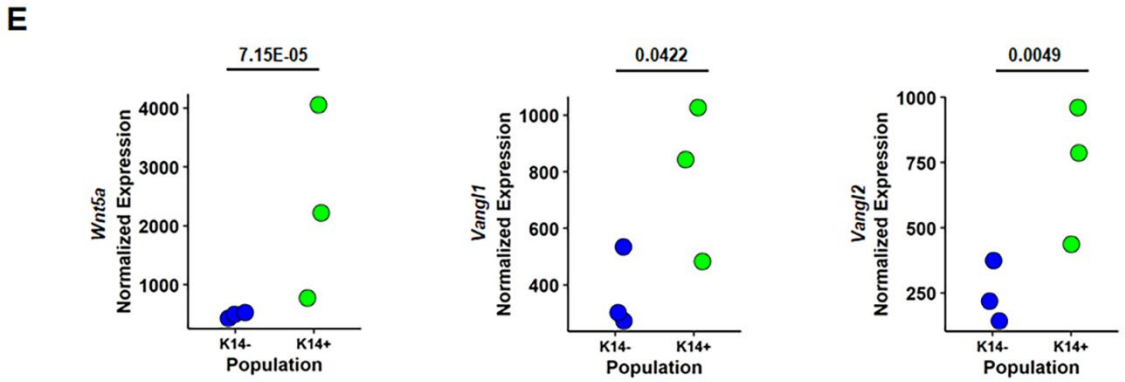

Figure 4. Wnt/PCP signaling drives collective cell invasion *ex vivo* and is upregulated in the K14-positive leader cell population. A Representative bright field images of *MMTV-PyMT*-derived mouse mammary tumor organoids stably overexpressing Vector, Vangl1, Vangl2 or Wnt5a invading into collagen in the presence of 2.5nm *b*FGF. **B** Quantification of the percentage of organoids counted with 0-2, 3-5, and 6+ collectively invading protrusions for Vector-, Vangl1-, Vangl2-, or Wnt5a-expressing organoids (Vector 547, Vangl1 371, Vangl2 276, Wnt5a 456 organoids counted from n=6 independent experiments, p-values represent Vector (V) vs Vangl1 (V1), Vangl2 (V2), Wnt5a (W), 0-2 protrusions; V vs V1 p=0.0011, V vs V2 p=6.32E-06, V vs W p=2.50E-05, 3-5 protrusions; V vs V1 p=0.0001, V vs V2 p=8.94E-05, V vs W p=0.0092, 6+ protrusions; V vs V1 p=0.0027, V vs V2 p=0.0132, V vs W p=0.0024). Bar graphs represent the mean ± sem of experimental replicates (n), significance was determined by a two-sided unpaired t-test, *p < 0.05, **p < 0.01, ***p < 0.001, ****p < 0.0001. **C** Representative confocal images of Vector-, Vangl1-, Vangl2-, or Wnt5a-expressing PyMT-derived organoids stained with K14: green, Actin: red, and DAPI: blue. Yellow arrows: K14+ collectively invading protrusion. **D** Representative confocal images of PyMT-derived organoids stained with K14: green, Vangl1: red, Actin: grey, and DAPI: blue (top) and boxed regions have been expanded to show details (bottom). Yellow arrows: K14+/Vangl1+ leader cells of a collectively invading protrusion. **E** Analysis of RNA-sequencing data set SRP066316 from NCBI Sequence Read Archive for *Wnt5a, Vangl2,* and *Vangl1* transcript in K14- and K14+ cells derived from *MMTV-PyMT* tumors (*Wnt5a* p= 7.15E-05, *Vangl2* p=0.0049, *VANGL1* p=0.0422), significance was determined by likelihood ratio test followed by Benjamin-Hochberg correction for multiple hypothesis testing. Scale bars=50μm.

299 specifically augments the protrusive activity of K14-positive leader cells that drive collective
300 invasion. In support of our findings, analysis of a publicly available dataset that accompanied the
301 foundational study describing the contributions of K14-positive leader cells to breast cancer
302 progression (Cheung et al., 2016) revealed that *Wnt5a*, *Vangl1,* and *Vangl2* transcripts are
303 significantly elevated in the K14-positive tumor cell population (Figure 4E). Other Wnt/PCP
304 component transcripts including noncanonical Frizzled receptors and Dvl were not significantly
305 altered (Figure 4–figure supplement 1E). Taken together, these findings suggest that Wnt/PCP
306 signaling may augment the invasive behavior of K14-positive leader cells and supports a model
307 in which Vangl-mediated Wnt/PCP signaling drives metastatic dissemination through promotion
308 of local collective cell migration and invasion from the primary tumor.
309
310 *Vangl localizes to the leading-edge of collectively migrating breast cancer cells and promotes a*
311 *hyper-protrusive leading-edge*
312 Wnt/PCP signaling is essential for the establishment and maintenance of polarity in epithelial
313 tissues, where it regulates cell polarization in the planar axis across the surface of an epithelial
314 sheet (Devenport, 2014). Planar polarity across the tissue is achieved through the asymmetric
315 distribution of core Wnt/PCP complexes within individual cells reinforced by intracellular
316 antagonism between opposing complexes (Axelrod, 2001; Jenny et al., 2005; Tree et al., 2002;
317 Warrington et al., 2017). Intercellular complexes formed by opposing complexes on adjacent cells
318 then transmit that asymmetry to neighboring cells (Chen et al., 2008; Strutt & Strutt, 2008; Wu &
319 Mlodzik, 2008), and propagation of this asymmetry across many cell distances allows for
320 integration of global cues to locally polarized cellular behavior (Devenport, 2014). However, the
321 requirement for Wnt/PCP complex asymmetry in migrating cancer cells has remained unclear,
322 despite significant effort to understand component localization in migrating breast cancer cells
323 (Anastas et al., 2012; Daulat et al., 2016; Luga et al., 2012).
324

We employed immunofluorescence microscopy to assess the localization of endogenous Wnt/PCP components in MCF7 breast cancer cells and cells derived from *MMTV-PyMT* tumors, which migrate as cohesive sheets with E-cadherin-rich cell-cell junctions (Figure 5–figure supplement 1A,B). In MCF7 cells, we observed that both Vangl1 and Fzd7, which typically localize to opposing complexes within planar polarized tissues (VanderVorst et al., 2018), co-localize at actin-rich migratory protrusions in cells at the leading-edge of a collectively migrating cohort (Figure 5A). Consistent with observations that Vangl overexpression enhances cellular motility (Figure 3C,D), Vangl1 overexpression in MCF7 cells elicits a hyper-protrusive leading-edge enriched for Vangl1, Fzd7 and Actin (Figure 5B), suggesting that elevated Vangl1 mediates the assembly of Wnt/PCP complexes that promote the formation of pro-migratory protrusions that drive collective cell migration. Indeed, elevated Vangl1 expression significantly increases both the number of Vangl1-rich protrusions in leader cells and the percentage of leader cells with Vangl1-rich protrusions in a collectively migrating sheet of MCF7 cells (Figure 5–figure supplement 1C,D). We also observed Vangl1-rich protrusions at the leading-edge of collectively migrating primary *MMTV-PyMT* tumor cells migrating as both sheets and clusters (Figure 5C). These data suggest that Vangl mediates the formation of pro-migratory protrusions in collectively migrating breast cancer cells and that high Vangl expression drives enhanced cellular invasiveness through the regulation of aberrant leading-edge protrusion formation.

Vangl2 regulates RhoA activity in leader cells of collectively migrating breast cancer cells

Our findings that Vangl drives collective cell motility and invasion as well as mediates the formation of pro-migratory protrusions in leader cells of collectively migrating breast cancer cells led us to question the molecular mechanisms by which Vangl achieves these outcomes. We hypothesized that Vangl may regulate the actin cytoskeleton in leader cells via engagement of Rho GTPases Rac1 and RhoA, which are engaged in Wnt/PCP-mediated motility during vertebrate gastrulation in developing embryos (Habas et al., 2003; Habas et al., 2001). The

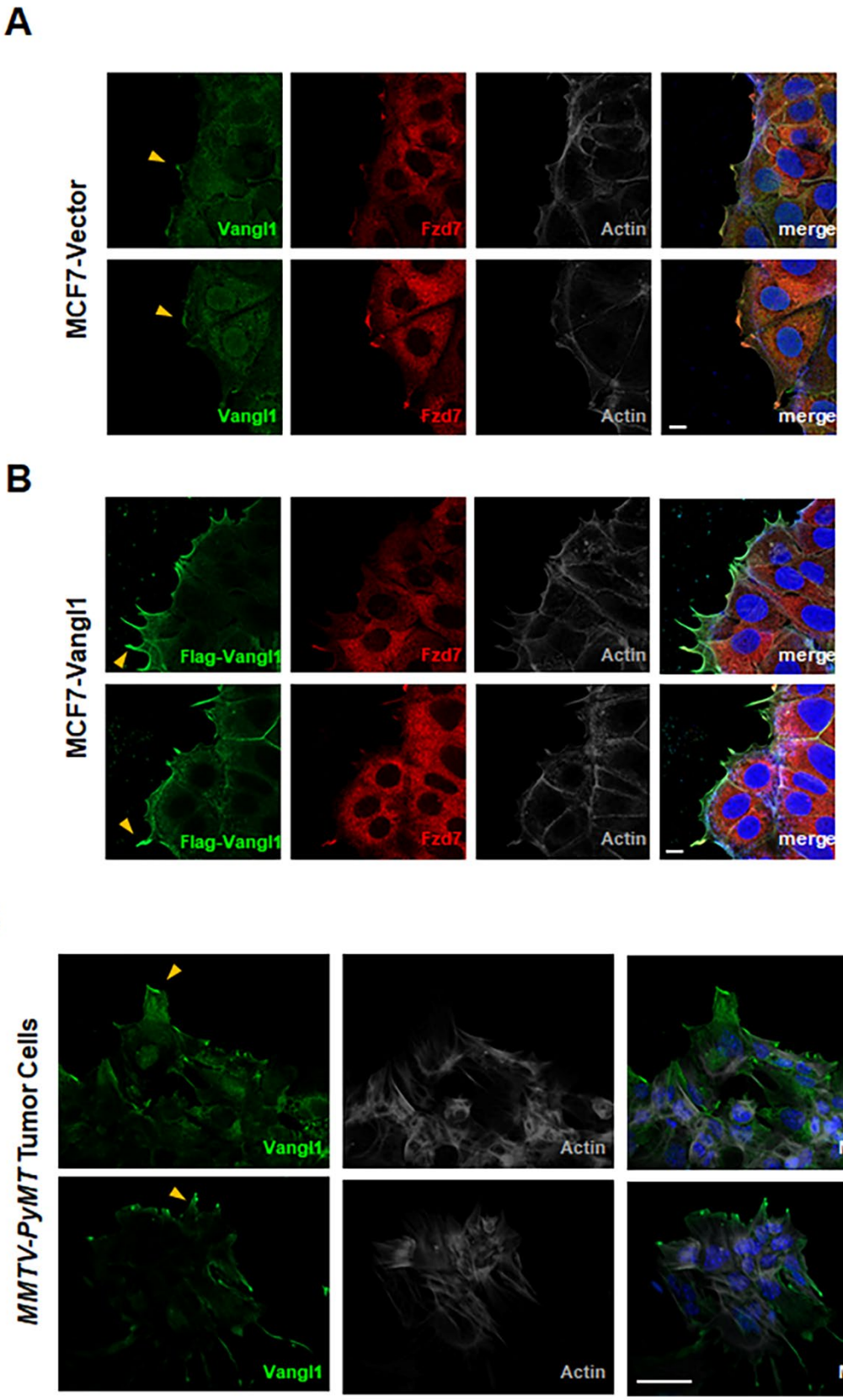

Figure 5. Vangl localizes to the leading-edge of leader cells in collectively migrating breast cancer cells and promotes a hyper-protrusive morphology. A,B Representative confocal images of collectively migrating MCF7-Vector cells stained for Vangl1: green, Fzd7: red, Actin: grey, and DAPI: blue **(A)** and MCF7-Flag-Vangl1 cells stained for Flag: green, Fzd7: red, Actin: grey, and DAPI: blue **(B)**, yellow arrows: Vangl1-rich protrusions, scale bar=10μm. **C** Representative confocal images of *MMTV-PyMT* tumor-derived cells migrating collectively as a sheet (upper panel) or as a cluster (lower panel) stained for Vangl1: green, Actin: grey, and DAPI: blue. Yellow arrows: Vangl1-rich protrusions in leading-edge cells of migrating sheets and clusters, scale bar=50μm.

regulation of Rac1 and RhoA GTPase activity is complex and permits context-specific activation of signaling events at specific subcellular localizations with precise kinetics (Ridley, 2015). Unfortunately, previous studies that investigated the ability of Wnt/PCP components to specifically engage and regulate Rho GTPases in cancer cells have predominantly assessed global GTPase activity in lysed cells via GST pull-down assays (Asad et al., 2014; Kurayoshi et al., 2006; Wald et al., 2017), leaving the localization and kinetics of Wnt/PCP-mediated RhoA and Rac1 activity largely unexplored.

We investigated the spatiotemporal dynamics of GTPase signaling in real time via time-lapse imaging in collectively migrating breast cancer cells by monitoring GTPase activity using stably expressed Rac1 or RhoA fluorescence resonance energy transfer (FRET) biosensors (Yang et al., 2016). Here, MCF7 cells stably expressing non-targeting control shRNA or two independent *VANGL2*-targeted shRNAs and a Rac1 or RhoA biosensor were seeded onto glass-bottom plates, the confluent monolayer was scratched at zero hours, and scratches imaged every fifteen minutes throughout the 12 hour migration assay (Figure 6A, Supplementary Videos 1-3). The mean FRET ratio, which indicates Rac1 or RhoA activity, was measured after 1, 6, and 12 hours of migration and plotted as a function of distance from the leading-edge of the migrating cohort of MCF7 cells using a custom MATLAB script to quantify Rac1 and RhoA activity across the monolayer of cells (Figure 6B, Figure 6–figure supplement 1A). Briefly, our MATLAB script identified the leading-edge of the migrating cohort of MCF7 cells (Figure 6–figure supplement 1B) and binned migrating cells based on their distance from the edge of the scratch (Figure 6–figure supplement 1C).

Spatial analysis of RhoA activity after one hour of migration revealed that RhoA activity is highest in the leading-edge cells, with activity peaking at approximately 5-10μm from edge of the scratch (Figure 6B) in a collectively migrating cohort of MCF7 cells. Indeed, RhoA activity is significantly higher 5μm from the edge of the scratch as compared to cells 100μm from the edge of the scratch

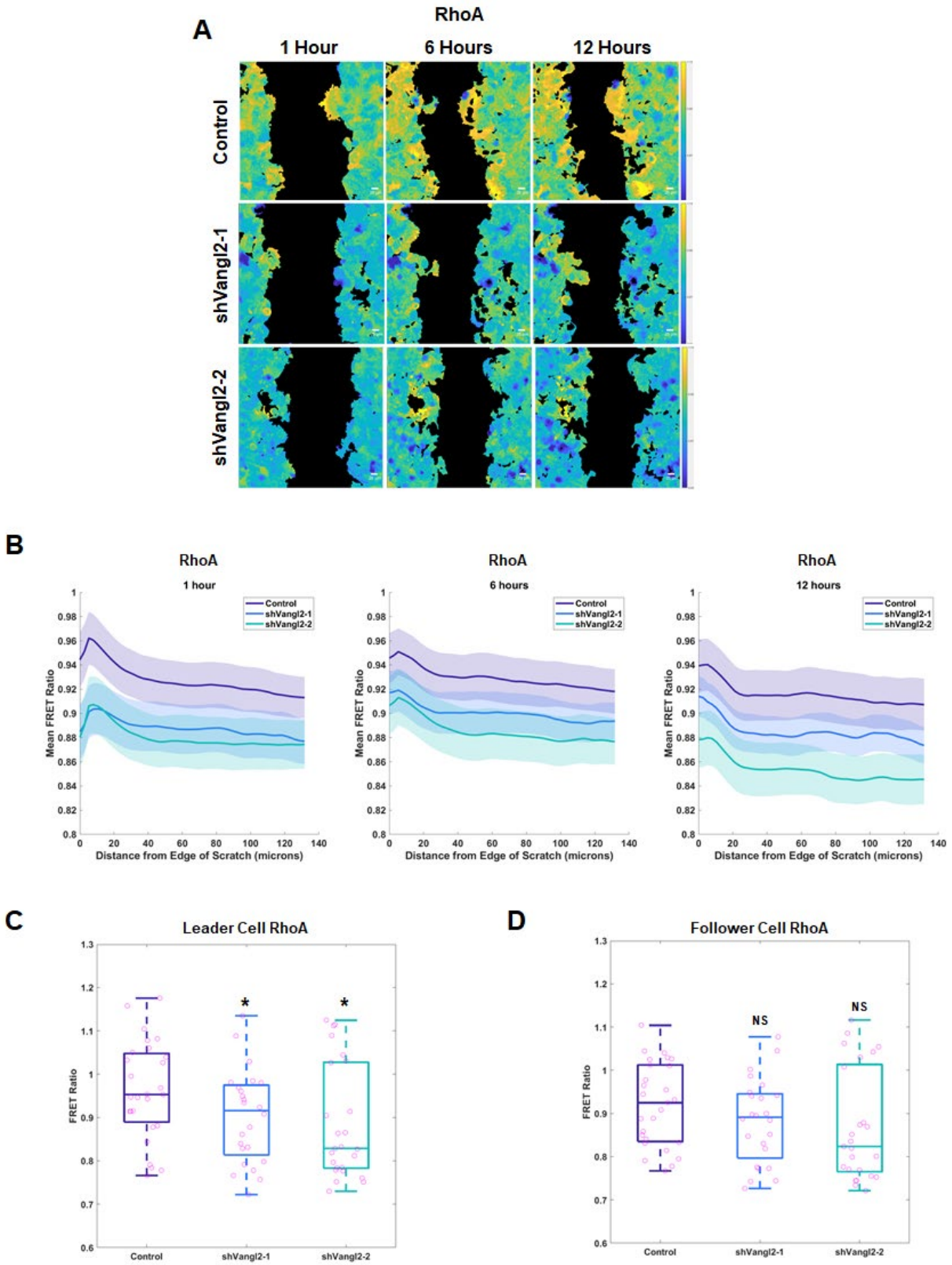

388

Figure 6. Vangl2 preferentially regulates RhoA activity in leader cells of collectively migrating breast cancer cells. A Representative spatial activity profiles of RhoA in collectively migrating MCF7 cells stably expressing RhoA-FRET biosensor and Control (top row), shVangl2-1 (middle row), or shVangl2-2 (bottom row) at 1 hour (left column), 6 hours (center column), and 12 hours (right column. Color bars indicate the range of RhoA-FRET biosensor ratios. Scale bar=25μm. **B** RhoA activity as a function of distance in μm from the leading-edge of collectively migrating MCF7 cells stably expressing Vector (*n*=27 wells), shVangl2-1 (*n*=24 wells), or shVangl2-2 (*n*=25 wells) at 1, 6, and 12 hours of migration, error bars indicate ± sem. **C,D** RhoA activity after one hour of migration at 5μm **(C)** and 100μm **(D)** from the leading-edge of collectively migrating MCF7 cells stably expressing Vector, shVangl2-1 (Vector vs shVangl2-1, 5μm p=0.05, 100μm p=0.1803), or shVangl2-2 (Vector vs shVangl2-2, 5μm p=0.0271, 100μm p=0.1094), significance was determined by a two-sided unpaired *t*-test.

after one hour of migration (Figure 6–figure supplement 1D). MCF7 cells are roughly 20-25μm in diameter, thus the elevated RhoA near the scratch edge likely represents leader cells. Depletion of *VANGL2* significantly reduced RhoA activity in leader cells 5μm from the edge of the scratch (Figure 6C) and appeared to reduce RhoA activity in follower cells 100 μm from the edge of the scratch, but did not pass our threshold for statistical significance (Figure 6D) after one hour of migration. Rac1 signaling did not differ spatially within the migrating cohort and modulation of *VANGL2* did not alter Rac1 activity (Figure 6–figure supplement 1A). Collectivly, these findings suggest that Vangl2-dependent Wnt/PCP signaling specifically regulates RhoA in leader cells to support actin cytoskeletal rearrangements critical to the formation of pro-migratory protrusions that drive collective migration.

Mechanistically, our observations demonstrate that Vangl2 acts at the leading edge of collectively migrating cells to prompt the RhoA-dependent cytoskeletal dynamics necessary for pro-migratory cellular protrusion formation (Figure 7). By extension, we propose that the high Vangl expression frequently observed in primary tumors drives aberrant Vangl-dependent Wnt/PCP signaling, resulting in a hyper-protrusive leading-edge that supports invasiveness and ultimate metastatic dissemination.

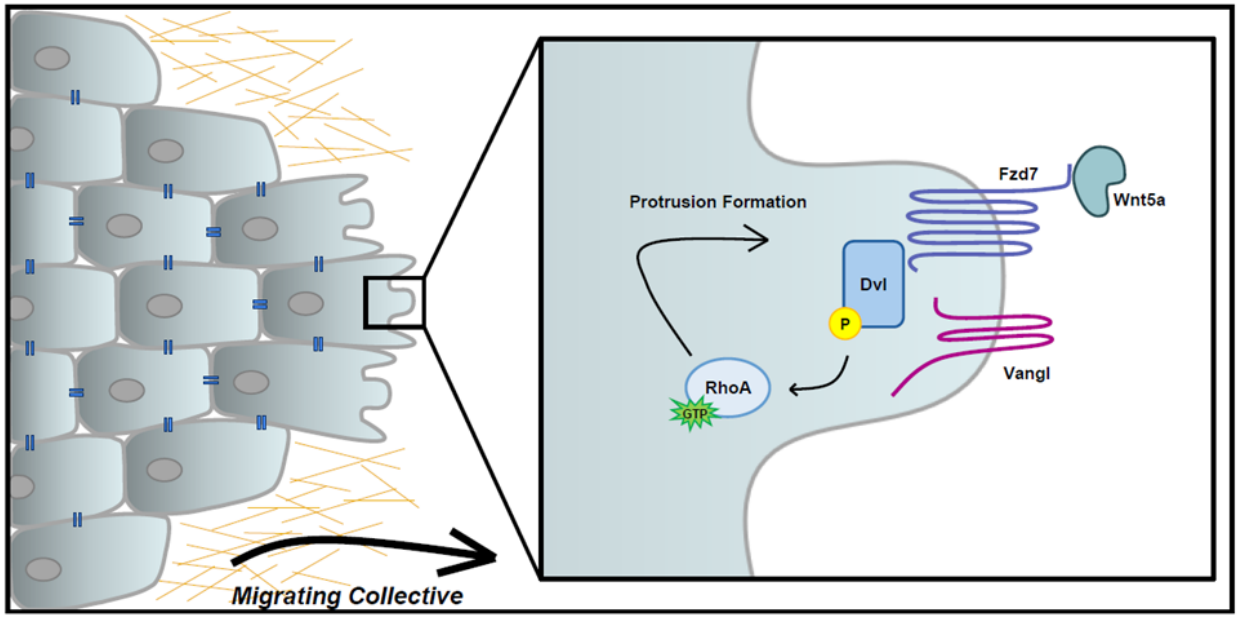

Figure 7. Model of Vangl-dependent Wnt/PCP signaling mediating breast cancer cell collective migration and invasion. Vangl2 acts at the leading edge of collectively migrating cells to prompt the RhoA-dependent cytoskeletal dynamics necessary for pro-migratory cellular protrusion formation.

Discussion

Metastatic disease is responsible for the majority of cancer-related deaths (Steeg, 2016), despite significant investment into elucidating molecular drivers of metastasis and identifying opportunities for therapeutic intervention. The acquisition of migratory and invasive behaviors by tumor epithelial cells is a critical step for metastatic dissemination, but the molecular mechanisms underlying this transition remain incompletely described. However, tumor cells commonly reactivate and exploit developmental motility programs to promote malignancy, giving rise to invasiveness, metastasis, and poor patient survival (Friedl & Gilmour, 2009). In this study, we demonstrate that Wnt/PCP signaling, which in embryos promotes cell polarity and motility to regulate proper tissue structuring (Devenport, 2014), drives the collective migration and invasion of breast tumor cells. We show that the Wnt/PCP-specific transmembrane scaffold protein Vangl2 is vital for the efficient formation of metastatic lung lesions from ErbB2-driven mammary tumors, and localizes to the leading-edge of cohorts of collectively migrating breast cancer cells where it engages RhoA to drive the formation of pro-migratory protrusions.

Despite reports that Vangl2 is highly expressed in 25% of invasive breast cancers (Hatakeyama et al., 2014) and that elevated *VANGL2* correlates with advanced stage disease and decreased metastasis-free survival of breast cancer patients (Puvirajesinghe et al., 2016), the functional role of Vangl2 in breast cancer malignancy has remained largely unexplored. Here, we present the novel finding that that Vangl2, a critical component of Wnt/PCP signaling, is vital to efficient metastasis of mouse mammary tumors. Loss of *Vangl2* does not impact the efficiency with which disseminated tumor cells colonize the lung nor the proliferation of established metastatic lesions. We instead find that high Vangl expression drives collective cell migration *in vitro* and collective cell invasion *ex vivo,* and elevated *Vangl1* and *Vangl2* expression in K14-positive invasive leader cells *in vivo*. High Vangl expression results in hyper-protrusive leading-edge morphology within leader cells of collectively migrating cohorts suggesting that Wnt/PCP signaling is critical in

promoting the cytoskeletal remodeling necessary for the invasive behavior of primary breast tumor cells. Our data indicate that Vangl2 contributes to local collective and migration within the primary tumor, consistent with its role in mediating cell motility during embryonic development (Butler & Wallingford, 2017), resulting in increased dissemination from the primary tumor.

While *Vangl2* is critical for metastasis of *MMTV-NDL* tumors, it is dispensable for both the initiation and growth of the primary tumor. Our observations are consistent with a role for Vangl2 in mediating cell motility events critical to developing embryos (Butler & Wallingford, 2017; Devenport, 2014), but conflict with a previous report in which shRNA-mediated knockdown of *VANGL2* decreased proliferation of SUM159 and HCC1806 breast cancer cells xenografted into the flanks of NSG mice (Puvirajesinghe et al., 2016). Based on reports that *VANGL2* upregulation is associated with higher grade breast tumors (Puvirajesinghe et al., 2016), we hypothesize that elevated *VANGL2* expression and resulting activation of Wnt/PCP signaling is a feature of late-stage or advanced disease. Because the autochthonous *MMTV-NDL* model recapitulates the full course of breast cancer development beginning from an untransformed mammary epithelial cell, Wnt/PCP signaling may have not yet been aberrantly engaged for the majority of primary tumor growth. Xenograft tumors derived from cell lines models of late-stage breast cancer may more heavily rely upon Wnt/PCP signaling for primary tumor growth. This discrepancy suggests that Wnt/PCP signaling may be a marker that could be used clinically to predict invasive or aggressive breast cancer.

Our finding that elevated Vangl protein mediates phosphorylation of Dvl2, a critical effector of downstream Wnt/PCP signaling, led us to speculate that Vangl may directly regulate actin cytoskeleton rearrangements in leader cells. Both the Rho GTPases Rac1 and RhoA are essential components of Wnt/PCP signaling-mediated motility during embryonic development (Habas et al., 2003). To investigate Rho GTPase spatiotemporal dynamics during breast cancer collective

cell migration, we employed time-lapse microscopy of MCF7 cells stably expressing FRET biosensors for Rac1 and RhoA. We measured the spatial activity of each GTPase as a function of distance from the edge of a scratch in the cellular monolayer throughout a 12-hour scratch migration. We found RhoA activity consistently peaks in leader cells, whereas Rac1 has a more uniform spatial activity pattern across both leader and follower cell populations. Observation of elevated RhoA activity in MCF7 leader cells was somewhat surprising, as leader cells in collective cell migration are generally thought to have high Rac activity at the cell front to coordinate membrane protrusions via branched actin polymerization, while high RhoA activity at the cell rear facilitates acto-myosin based contraction (Karlsson et al., 2009; Mayor & Etienne-Manneville, 2016; Zegers & Friedl, 2014). However, spatial patterning of Rac1 and RhoA activity appear to be specific for both cell migration mode and cell type. For example, in individual migrating normal kidney epithelial Ptk1 cells, RhoA plays a central role in driving anterograde actin flows and contractile forces on strong focal adhesions at the cell front, which work to pull the cell forward (Gupton & Waterman-Storer, 2006). In collectively migrating Madin-Darby Canine Kidney (MDCK) cells, thick actin-myosin II cables around the perimeter of protrusive cell collections termed 'fingers' and RhoA activity highest in leading-edge cells regulating the acto-myosin cable (Reffay et al., 2014). Future work is required to determine if collectively migrating MCF7 cells, or collectively migrating breast cancer cells more generally, develop acto-myosin cables analogous to MCDK cells.

Our findings provide substantive insight into the mechanism by which Vangl proteins specifically mediate the formation of pro-migratory protrusions at the leading-edge of leader cells in collectively migrating cohorts. Additionally, these data suggest that Vangl-mediated regulation of RhoA dynamics in leader cells is critical to Wnt/PCP-mediated collective cell migration and invasion. However, the molecular underpinnings of Vangl-mediated RhoA activity within leader cells are not clear. In vertebrate gastrulation, Wnt/PCP signaling appears to drive cellular motility

via engagement of Rho family GTPases in a manner that depends on both the cytoplasmic effector Dvl and Daam1, a Formin homology protein that mediates Wnt-induced Dvl-Rho complexes (Habas et al., 2001). While this study did not investigate whether Vangl is a required component of this complex, we speculate that Vangl may serve as a required scaffold upon which the Dvl-Daam1-RhoA complex assembles in leader cells. This is consistent with previous reports suggesting that Vangl may be a master scaffold upon which diverse complexes assemble (Anastas et al., 2012; Puvirajesinghe et al., 2016; Wald et al., 2017). These findings, coupled with our observations that Vangl localizes to leader cells in collectively migrating and invading cohorts and drives the formation of pro-migratory protrusions, suggests that Vangl-RhoA-mediated modulation of the cytoskeleton in leader cells is a significant contributor to the invasive nature and metastatic dissemination of primary tumor cells.

Materials & Methods

Generation of Vangl2/NDL mice. All experimental protocols were approved by the IACUC of the University of California, Davis, CA, USA. *Vangl2*$^{tm2.1Mdea}$*/J* conditional knockout mice (Copley et al., 2013) (The Jackson Lab, Stock #025174) were crossed with *Tg(MMTV-cre)4Mam/J* mice (Wagner et al., 1997) (The Jackson Lab, Stock #003553) to generate mice with Vangl2 deletion in the mammary gland. The *MMTV-NDL* mouse has been previously described (Siegel et al., 1999). Genotypes were confirmed by polymerase chain reaction in house using primers for Vangl2 (Fwd 5'-CAGAA CCTCCTGTCCCTGA-3'; Rev 5'-CTCAGCTAAACCACCTCTGC-3'), Cre (Fwd 5'-GCGGTCTGGCAGTAAAAACTATC-3'; Rev 5'-GTGAAACAGCATTGCTGTCACTT-3'), and NDL (Fwd 5'-TTCCGGAACCCACATCAG -3'; Rev 5'- GTTTCCTGCAGCAGCCTA -3').

Tumor monitoring and analysis. Mammary tumors were palpated once or twice weekly in female Vangl2/NDL mice commencing at 16 weeks of age by a single investigator and all palpable tumors were measured by calipers. When the largest tumor reached 2cm in any direction, mice were euthanized by CO_2 asphyxiation and tumors were collected and either fixed in 10% neutral buffered formalin for paraffin embedding and sectioning or further dissociated for *in vitro* analysis. Mice with illnesses arising independent of their tumors that required sacrifice prior to reaching the pre-determined endpoint were excluded from analyses.

Histology and Immunohistochemistry. Histologic analysis of lungs was performed for all mice on study (n=20 per genotype) and for a randomly selected subset of Vangl2$^{+/+}$/NDL and Vangl2$^{fl/fl}$/NDL mammary tumors (n=4 per genotype). H&E-stained sections were prepared using previously described methods (Rowson-Hodel et al., 2015). Immunohistochemistry (IHC) was performed as previously described (Rowson-Hodel et al., 2018). An internal negative control (no primary antibody) was included with each assay.

Lung metastases analysis. Lungs were inflated with PBS, fixed in 10% neutral buffered formalin, paraffin embedded, and sectioned for IHC analysis and H&E staining. The number of ErbB2-positive metastatic lesions present on all five lung lobes were counted for all mice on study (n=20 per genotype) from images taken on a Keyence BZ-X810 microscope. Metastatic burden was quantified by normalizing the number of metastatic lesions to the total tumor burden.

Tail vein injections. Pooled primary Vangl2$^{+/+}$/NDL and Vangl2$^{fl/fl}$/NDL mammary tumors (Vangl2$^{+/+}$/NDL *n*=11, Vangl2$^{fl/fl}$/NDL *n*=10; 5 x 10^5 in 200 µL PBS) were instilled to the lateral tail vein of 12-week-old FvB/NJ mice. Lungs were harvested 6-weeks post injection and analyzed for metastatic lesions. Mice were randomly assigned to cohorts and were caged as mixed cohorts.

Cell culture and reagents. BT549, HCC1937, HCC38, MCF7, MDA-MB-157, MDA-MB-231, MDA-MB-468, nMuMG, L-Cells, and L-Cells-Wnt3a, and HEK293T cells were purchased from the American Type Culture Collection (ATCC) and maintained as recommended at 37°C in 10% CO_2 in media supplemented with 10% fetal bovine serum (FBS, Genesee Scientific), 1% penicillin-streptomycin (Invitrogen). Met-1 (gifted by A.D. Borowsky) and NDL cells were maintained as previously described(Borowsky et al., 2005; Miller et al., 2008). Prior to use, cell lines were authenticated by short-tandem repeat profiling (Genetics Core Facility; University of Arizona, Tucson, AZ, USA) and tested for mycoplasma contamination by RT-PCR as described (Uphoff & Drexler, 2002, 2004). Antibodies used for immunoblotting, immunofluorescence, and immunohistochemistry are as follows: anti-Dvl2, anti-p-β-Catenin (Ser33/37/Thr41), anti-β-Catenin (Cell Signaling), anti-Tubulin (Sigma), horseradish peroxidase-conjugated goat anti-mouse and goat anti-rabbit secondary antibodies (Bio-Rad), anti-Vangl1 (R&D Systems), anti-Fzd7 (Abcam), anti-Keratin14 (Biolegend), anti-E-Cadherin, anti-Flag and anti-V5 (Cell Signaling), anti-Phalloidin647 (Invitrogen), and AlexaFluor 488-conjugated goat anti-mouse, AlexaFluor 546-conjugated goat anti-rabbit, and Alexa-Fluor 568-conjugated goat anti-chicken

565 secondary antibodies (Invitrogen), and anti-Ki67, anti-c-Caspase3, and anti-ErbB2 (Cell
566 Signaling). Cells were treated with the Wnt-inhibitor C59 at 100nM (R&D Systems).
567
568 **Generation of stable overexpression and knockdown cell lines by lentiviral transduction.**
569 *VANGL2*-targeted shRNA constructs shVangl2-1 (ID: V3LHS_334647 or ID: TRCN0000180101),
570 shVangl2-2 (ID: V3LHS_334648 or TRCN0000417141) (Dharmacon, Sigma-Aldrich), or control
571 vectors pGIPZ (Dharmacon) or pLKO.1 (a gift from David Sabatini, Addgene plasmid #1864;
572 http://n2t.net/addgene:1864 ; RRID:Addgene_1864) were employed for Vangl2-depletion studies.
573 Stable overexpression cells were created using Vangl1 and Vangl2 plasmids (Harvard PlasmID
574 repository, HsCD00339551 and HsCD00294893) and Wnt5a plasmid that was a gift from Marian
575 Waterman (Addgene plasmid # 35911; http://n2t.net/addgene:35911 ; RRID:Addgene_35911)
576 subcloned into the control vector pLX304, a gift from David Root (Addgene plasmid # 25890;
577 http://n2t.net/addgene:25890 ; RRID:Addgene_25890). VSVG-pseudotyped lentivirus was
578 generated by transfecting HEK293T cells with the psPax2 packaging vector. Cells were
579 transduced with 10µg/mL polybrene (Millipore), followed by drug selection with 1µg/mL Puromycin
580 (Sigma-Aldrich) or 4µg/mL Blasticidin (Sigma-Aldrich).
581
582 **Wnt5a and Wnt3a stimulation.** Wnt5a conditioned media was produced by stably transducing
583 nMUMG, MCF7, MDA-MB-231, MDA-MB-468, or NDL cells with Vector- or Wnt5a-containing
584 lentivirus. Vector- or Wnt3a- conditioned media was collected from L-Cell and L-Cell-Wnt3a,
585 respectively. Conditioned media was collected from confluent cell culture plates, cleared of debris
586 by centrifugation, and stored at -80°C.
587
588 **Scratch migration assays.** Confluent monolayers of cells were scratched with a sterile pipette
589 tip and imaged immediately and after twelve hours with an Olympus IX81 microscope with
590 CellSens Entry software. Scratch area was measured using ImageJ (NIH) and the area of the

scratch filled in over twelve hours was quantified. Results were normalized to appropriate controls for each assay.

Immunoblotting. Cells were washed with 1X PBS and lysed directly in 2x Laemmli sample buffer. All samples were resolved by SDS-PAGE, transferred to nitrocellulose membranes, and blotted with the indicated antibodies. Immunoblots were developed using Pierce SuperSignal West chemicals (Thermo Fisher) on an AlphaInnotech imaging station and quantified with ImageJ (NIH).

Real-time PCR analysis. RNA was collected using a PureLink RNA MiniKit (Ambion) and converted to cDNA with the High-Capacity cDNA reverse transcription kit (Applied Biosystems). *q*PCR was conducted in a Bio-Rad CFX96 real-time PCR system using TaqMan gene-specific primer/probe sets (Applied Biosystems) and SsoAdvanced master mix (Bio-Rad). Analysis was conducted using Bio-Rad CFX Manager software and message levels were normalized to GAPDH.

***Ex vivo* 3D organoid invasion assays.** *MMTV-PyMT* tumor samples were a kind gift from Dr. Jason Hatakeyama (Stanford University, Stanford, CA, USA). Tumors were dissociated into single cells as previously described(Diehn et al., 2009) with minor modifications and seeded in Matrigel (Corning) with organoid growth media, which has been previously described (Nguyen-Ngoc et al., 2012). After twenty-four hours in Matrigel, cells were transduced with specified lentivirus and spinfected for one hour at ~500G in a Beckman centrifuge. After seven days in culture, organoids derived from single *MMTV-PyMT* tumor cells were recovered from Matrigel using Cell Recovery Solution (Corning) and embedded into rat-tail collagen I (Thermo Fisher) as previously described (Nguyen-Ngoc et al., 2012). Invasive protrusions were imaged and counted with an Olympus IX81 microscope with CellSens Entry software or Zeiss LSM 710 AxioObserver confocal microscope.

RNA-seq data mining. Raw RNAseq reads from Cheung et al., archived as SRP066316 was downloaded from the Sequence Read Archive (Cheung et al., 2016). Reference genome for pseudoalignment was built in Kallisto v0.43.1 from Genome Reference Consortium Mouse Build 38 using a k-mer length of 31. Reads were then pseudoaligned to the reference genome using 100 bootstraps to estimate error. Differential expression analysis was then performed in R using the DESeq2 package (1.28.1). Biological replicate #3 (SRR291722 and SRR2921727) varied considerably from the other replicates by principal component analysis and expression of key marker genes, and was therefore omitted from the analysis.

Immunofluorescence microscopy. Cells were seeded onto coverslips, fixed with 4% paraformaldehyde, and stained as indicated. PyMT-derived organoids embedded in collagen I were fixed with 4% PFA and stained as indicated. Imaging was conducted on a Zeiss LSM 710 AxioObserver confocal microscope or Keyence BZ-X810 microscope. An internal negative control (no primary antibody) was included with each assay. Average number of Vangl1-rich protrusions/cell was quantified by counting the number of Vangl1+ protrusions in leader cells along the leading-edge of a MCF7 cells actively migrating into a scratch made in a confluent monolayer from 4 or 8 independent scratch assays. Percentage of cells with Vangl1-rich protrusions was quantified by counting the number of leader cells with and without Vangl1+ protrusions along the leading-edge of MCF7 cells actively migrating into a scratch made in a confluent monolayer from 4 or 8 independent scratch assays.

FRET biosensor scratch assay imaging. Rac1 and RhoA intramolecular FRET biosensors and have been previously described (Itoh et al., 2002). MCF7 cells stably expressing *VANGL2*-targeted shRNAs to deplete Vangl2 were stably transfected with Rac1 or RhoA intramolecular FRET biosensors using PEI transfection reagent. Rac1 or RhoA biosensor expressing cells were

643 sorted with a BD “inFlux” 18-color cell sorter (Becton Dicksinson). For all imaging experiments,
644 cells were plated on glass-bottomed 96-well plates (Cellvis) and grown to confluency. Prior to
645 imaging, the monolayers were scratched with a sterile pipette tip, and the media was replaced
646 with Liebovitz-15 (L-15) media, which was made with no riboflavin, folic acid or dyes to reduce
647 autofluorescence from the media supplemented with 2% FBS (UC Davis Biological Media
648 Services). The plates were then transferred to a Nikon Eclipse TI equipped with an OKO Labs
649 cage incubator set to 37 °C. The microscope is controlled by MATLAB (version 2015 A) through
650 Micro-Manager (v 1.6), allowing precise, repeatable experiments. The X & Y stage positions of
651 the scratch were identified by the user and all scratch positions were stored in MATLAB for time
652 lapse imaging. Epifluorescent CFP/YFP FRET images were collected every 15 min for 12 hours
653 using a 20x Nikon Apochromat 0.75 NA objective. Cyan (~440 nm) excitation illumination was
654 provided by the X-Cite XLED1 BLX module, while simultaneous acquisition of FRET images was
655 achieved using dual Andor Zyla 4.2 sCMOS cameras separated by a Cairn TwinCam LS image
656 splitter with a Chroma Technologies dichroic mirror (ZT491rdc) that reflects wavelengths less than
657 502nm to one camera, while passing longer wavelengths to the second camera.
658
659 **Camera and illumination corrections.** The dark-state noise for each camera was empirically
660 measured as described (Bell et al., 2021). In brief, several images were captured without
661 illumination and the microscope light path set to the oculars. The dark-state correction image was
662 generated by taking the median over the stack of dark images. This correction was then
663 subtracted from all experimental images. CFP/YFP FRET ratio images were observed to have a
664 gradient of activity from the top to the bottom of the images. A correction image was developed
665 to remove this gradient as described (Bell et al., 2021). Images of unstimulated, confluent
666 monolayers of MCF7 cells expressing the CFP/YFP FRET sensor were collected. FRET ratio
667 images were generated from raw CFP and YFP images that were processed using our standard
668 analysis pipeline. The median FRET ratio was taken over the stack of images on a pixel-by-pixel

basis. Only pixels that overlapped with a cell logical mask were included in the median analysis. To reduce local variability effects and noise, the median image was broken into 24x24 pixel blocks. Next, the median was taken for each block, the resulting image was then smoothed using a gaussian filter (sigma=5) and the image was then resized to match the size of the input image. To apply the correction, experimental FRET ratio images were divided by the ratio correction image.

Image alignment, background subtraction, segmentation, and speckle filtering. All image analysis methods were conducted using MATLAB. CFP/YFP FRET images were aligned using an alignment algorithm as described (Yang et al., 2016). Images were then cropped to ensure equal size. To estimate the background, empty wells containing L-15 media + 2% FBS were imaged with CFP/YFP imaging configurations that were identical to the experimental conditions. Eight empty well frames were collected, and the median was calculated on a per pixel basis over the image stack. The median well background images were then aligned and cropped to match the size of the experimental images. Next, the background mask was determined for the experimental images. To generate the background mask, the experimental images were log transformed to enhance the dimmer cell pixels. The image threshold was then calculated using Otsu's method (Otsu, 1979). The background logical mask was created by finding pixels in the log transformed image below the threshold. Pixels contained in the background mask were used to find the median intensity in both the empty well image and the experimental image. The ratio of the two median intensities was then used to scale the empty well image to match the intensity of the background pixels in the experimental image. Once scaled, the empty well images were subtracted from the experimental images to remove background.

To segment the cells for further processing, the scaled background image was subtracted from the CFP and YFP images. The CFP and YFP images were added to reduce signal to noise, and the sum image was then used to identify the cell mask and the scratch mask. Because the cell pixels were much brighter than the scratch pixels, the dimmest 0.5% of pixels were subtracted from the sum image, and the minimum pixel intensity value was set to 20 prior to log transformation. The log transformed images were rescaled to a pixel range from the first percentile to the ninetieth percentile and the background vs foreground threshold was identified using Otsu's method. Background pixels were identified below the threshold to create a background logical mask. The background mask was morphologically closed to remove small gaps in the mask. Small objects below 50 pixels in area were removed from the mask and small holes in the mask were filled. The inverse of this mask was used to define the cell mask. Both cell and background masks were saved for additional processing.

The raw CFP and YFP images from MCF7 cells had small, but very bright puncta. A speckle filter was developed to remove these puncta from the processed CFP and YFP images. The sum image of the two FRET channels was filtered using a Laplacian operator (alpha=0.9) to convert the brightest pixels to the smallest negative pixels. The Laplace filtered image was subtracted from the sum image, effectively making the brightest pixels even brighter. To threshold rare, but bright pixels, the histogram of the image was taken and the intensity value for the first bin with 9 or fewer pixels with positive intensity values were used as the threshold. A bright pixel binary mask was created for all pixels above the bright pixel threshold in the sum image. The bright pixel mask was then morphologically closed to connect neighboring pixels, and objects greater than 300 pixels were removed. Finally, the FRET reporters are plasma membrane associated, and in some circumstances, were bright enough to be captured by the bright pixel threshold. These objects were more linear as they were essentially tracings of cell edges. To remove these cell membrane objects, the eccentricity for each object was measured. Objects with an eccentricity

719 >0.6 (more linear than circular) were removed from the mask. The speckle mask was then saved
720 for processing the FRET ratio images.
721
722 Finally, to create the FRET ratio images, raw CFP and YFP images were background subtracted
723 using the scaled background image constructed above. For both CFP and YFP images, pixels in
724 the background mask and pixels in the speckle mask were set to NaNs to remove them from
725 further processing. The background subtracted and segmented CFP and YFP images were
726 smoothed with a gaussian filter (sigma=2) and saved for further processing. Next, the FRET ratio
727 was calculated by dividing the YFP image by the CFP imaged. The ratio correction image
728 described above was then applied to the FRET ratio image. These FRET ratio images were
729 written to movies and exported for later use.
730
731 **Computation of FRET ratios as a function of distance from the scratch edge.** To understand
732 whether cells near the scratch had higher GTPase activity when compared to cells in the
733 monolayer, FRET ratios were measured and binned based on their distance from the scratch
734 edge. To identify the scratch edge, the background masks described above were further
735 analyzed. The scratch is the largest object in the background mask, thus the object with the
736 maximum area was defined as the scratch mask. Next, all other objects in the background mask
737 were removed and the perimeter from the scratch mask was defined. The scratches were
738 consistently generated North to South on the well, thus pixels touching the top and bottom of the
739 perimeter mask image were removed, leaving two scratch edge perimeter masks that
740 corresponded with the left and right sides of the scratch. The scratch edges were then dilated by
741 2 pixels to ensure overlap with the edge of the cell mask defined above. Additionally, the cell
742 masks were separated based on their relative position to the scratch mask (Left or Right). The
743 MATLAB bwdistgeodesic function was then used to measure the “quasi-euclidean” distance of all
744 pixels in the left and right cell masks based on their distance from the corresponding scratch edge

mask. These distance masks were used to sort pixels into 5 μm bins based on their distance from the scratch edge. The ratio correction image was applied to the YFP images, then the mean intensity values for the background subtracted, and segmented FRET donor and FRET acceptor images were calculated for each bin. The mean FRET ratio for each bin was then calculated. These measurements were compiled for each well within the experimental groups and were used to generate the plots reported.

Statistical analysis. Prism software (GraphPad Software) was used for all statistical analyses. Statistical significance was determined by two-sided unpaired t-test with Welch's correction, paired t-test, Mann-Whitney test, Log-rank test, or likelihood ratio test followed by Benjamin-Hochberg correction for multiple hypothesis testing (indicated in the figure legends). *P*-values ≤ 0.05 were considered statistically significant.

Acknowledgements

These studies were supported by NIH grants R01CA230742 (KLC), F31CA210467 (KV), F31CA246900 (CD), F31CA165758 (JH), T32GM099608 (AB), and DP2HD094656 (SRC) and NSF Graduate Research Fellowship 1650042 (GRRB). We thank Henry Ho for discussion, reagents, and critical reading of the manuscript. We are grateful to Jonathan Van Dyke and the UCD Comprehensive Cancer Center Flow Cytometry Shared Resources supported in part by NIH grant P30CA093373 and Gabe Jackman at Keyence for their technical assistance.

Author Contributions

K.V., J.H., and K.L.C. contributed to conceptualization; K.V., J.H., G.R.R.B., S.R.C., and K.L.C. contributed to methodology; K.V., C.A.D., G.R.R.B., A.B., M.H., and H.L. contributed to data collection; K.V., C.A.D., J.H., G.R.R.B., S.R.C., and K.L.C. contributed to data analysis and interpretation; S.R.C. and K.L.C. contributed resources; K.V., J.H., G.R.R.B., and K.L.C. contributed to manuscript writing.

Competing Interests

The authors declare no competing interests.

References

Aceto, N., Bardia, A., Miyamoto, D. T., Donaldson, M. C., Wittner, B. S., Spencer, J. A., Yu, M., Pely, A., Engstrom, A., Zhu, H., Brannigan, B. W., Kapur, R., Stott, S. L., Shioda, T., Ramaswamy, S., Ting, D. T., Lin, C. P., Toner, M., Haber, D. A., & Maheswaran, S. (2014). Circulating tumor cell clusters are oligoclonal precursors of breast cancer metastasis. *Cell*, *158*(5), 1110-1122. https://doi.org/10.1016/j.cell.2014.07.013

Anastas, J. N., Biechele, T. L., Robitaille, M., Muster, J., Allison, K. H., Angers, S., & Moon, R. T. (2012). A protein complex of SCRIB, NOS1AP and VANGL1 regulates cell polarity and migration, and is associated with breast cancer progression. *Oncogene*, *31*(32), 3696-3708. https://doi.org/10.1038/onc.2011.528

Asad, M., Wong, M. K., Tan, T. Z., Choolani, M., Low, J., Mori, S., Virshup, D., Thiery, J. P., & Huang, R. Y. (2014). FZD7 drives in vitro aggressiveness in Stem-A subtype of ovarian cancer via regulation of non-canonical Wnt/PCP pathway. *Cell Death Dis*, *5*, e1346. https://doi.org/10.1038/cddis.2014.302

Axelrod, J. D. (2001). Unipolar membrane association of Dishevelled mediates Frizzled planar cell polarity signaling. *Genes Dev*, *15*(10), 1182-1187. https://doi.org/10.1101/gad.890501

Bell, G. R. R., Rincón, E., Akdoğan, E., & Collins, S. R. (2021). Optogenetic control of receptors reveals distinct roles for actin- and Cdc42-dependent negative signals in chemotactic signal processing. *bioRxiv*, 2021.2004.2003.438340. https://doi.org/10.1101/2021.04.03.438340

Belotti, E., Puvirajesinghe, T. M., Audebert, S., Baudelet, E., Camoin, L., Pierres, M., Lasvaux, L., Ferracci, G., Montcouquiol, M., & Borg, J. P. (2012). Molecular characterisation of endogenous Vangl2/Vangl1 heteromeric protein complexes. *PLoS One*, *7*(9), e46213. https://doi.org/10.1371/journal.pone.0046213

Borowsky, A. D., Namba, R., Young, L. J., Hunter, K. W., Hodgson, J. G., Tepper, C. G., McGoldrick, E. T., Muller, W. J., Cardiff, R. D., & Gregg, J. P. (2005). Syngeneic mouse mammary carcinoma cell lines: two closely related cell lines with divergent metastatic behavior. *Clin Exp Metastasis*, *22*(1), 47-59. https://doi.org/10.1007/s10585-005-2908-5

Bronsert, P., Enderle-Ammour, K., Bader, M., Timme, S., Kuehs, M., Csanadi, A., Kayser, G., Kohler, I., Bausch, D., Hoeppner, J., Hopt, U. T., Keck, T., Stickeler, E., Passlick, B., Schilling, O., Reiss, C. P., Vashist, Y., Brabletz, T., Berger, J., Lotz, J., Olesch, J., Werner, M., & Wellner, U. F. (2014). Cancer cell invasion and EMT marker expression: a three-dimensional study of the human cancer-host interface. *J Pathol*, *234*(3), 410-422. https://doi.org/10.1002/path.4416

Butler, M. T., & Wallingford, J. B. (2017). Planar cell polarity in development and disease. *Nat Rev Mol Cell Biol*, *18*(6), 375-388. https://doi.org/10.1038/nrm.2017.11

Caddy, J., Wilanowski, T., Darido, C., Dworkin, S., Ting, S. B., Zhao, Q., Rank, G., Auden, A., Srivastava, S., Papenfuss, T. A., Murdoch, J. N., Humbert, P. O., Parekh, V., Boulos, N., Weber, T., Zuo, J., Cunningham, J. M., & Jane, S. M. (2010). Epidermal wound repair is regulated by the planar cell polarity signaling pathway. *Dev Cell*, *19*(1), 138-147. https://doi.org/10.1016/j.devcel.2010.06.008

Carmona-Fontaine, C., Matthews, H. K., Kuriyama, S., Moreno, M., Dunn, G. A., Parsons, M., Stern, C. D., & Mayor, R. (2008). Contact inhibition of locomotion in vivo controls neural crest directional migration. *Nature*, *456*(7224), 957-961. https://doi.org/10.1038/nature07441

Chen, W. S., Antic, D., Matis, M., Logan, C. Y., Povelones, M., Anderson, G. A., Nusse, R., & Axelrod, J. D. (2008). Asymmetric homotypic interactions of the atypical cadherin flamingo mediate intercellular polarity signaling. *Cell*, *133*(6), 1093-1105. https://doi.org/10.1016/j.cell.2008.04.048

Cheung, K. J., Gabrielson, E., Werb, Z., & Ewald, A. J. (2013). Collective invasion in breast cancer requires a conserved basal epithelial program. *Cell*, *155*(7), 1639-1651. https://doi.org/10.1016/j.cell.2013.11.029

Cheung, K. J., Padmanaban, V., Silvestri, V., Schipper, K., Cohen, J. D., Fairchild, A. N., Gorin, M. A., Verdone, J. E., Pienta, K. J., Bader, J. S., & Ewald, A. J. (2016). Polyclonal breast cancer metastases arise from collective dissemination of keratin 14-expressing tumor cell clusters. *Proc Natl Acad Sci U S A*, *113*(7), E854-863. https://doi.org/10.1073/pnas.1508541113

Chu, C. W., & Sokol, S. Y. (2016). Wnt proteins can direct planar cell polarity in vertebrate ectoderm. *Elife*, *5*. https://doi.org/10.7554/eLife.16463

Copley, C. O., Duncan, J. S., Liu, C., Cheng, H., & Deans, M. R. (2013). Postnatal refinement of auditory hair cell planar polarity deficits occurs in the absence of Vangl2. *J Neurosci*, *33*(35), 14001-14016. https://doi.org/10.1523/JNEUROSCI.1307-13.2013

Daulat, A. M., Bertucci, F., Audebert, S., Serge, A., Finetti, P., Josselin, E., Castellano, R., Birnbaum, D., Angers, S., & Borg, J. P. (2016). PRICKLE1 Contributes to Cancer Cell Dissemination through Its Interaction with mTORC2. *Dev Cell*, *37*(4), 311-325. https://doi.org/10.1016/j.devcel.2016.04.011

Davey, C. F., & Moens, C. B. (2017). Planar cell polarity in moving cells: think globally, act locally. *Development*, *144*(2), 187-200. https://doi.org/10.1242/dev.122804

Devenport, D. (2014). The cell biology of planar cell polarity. *J Cell Biol*, *207*(2), 171-179. https://doi.org/10.1083/jcb.201408039

Diehn, M., Cho, R. W., Lobo, N. A., Kalisky, T., Dorie, M. J., Kulp, A. N., Qian, D., Lam, J. S., Ailles, L. E., Wong, M., Joshua, B., Kaplan, M. J., Wapnir, I., Dirbas, F. M., Somlo, G., Garberoglio, C., Paz, B., Shen, J., Lau, S. K., Quake, S. R., Brown, J. M., Weissman, I. L., & Clarke, M. F. (2009). Association of reactive oxygen species levels and radioresistance in cancer stem cells. *Nature*, *458*(7239), 780-783. https://doi.org/10.1038/nature07733

Ewald, A. J., Brenot, A., Duong, M., Chan, B. S., & Werb, Z. (2008). Collective Epithelial Migration and Cell Rearrangements Drive Mammary Branching Morphogenesis. *Developmental Cell*, *14*(4), 570-581. https://doi.org/https://doi.org/10.1016/j.devcel.2008.03.003

Fischer, K. R., Durrans, A., Lee, S., Sheng, J., Li, F., Wong, S. T., Choi, H., El Rayes, T., Ryu, S., Troeger, J., Schwabe, R. F., Vahdat, L. T., Altorki, N. K., Mittal, V., & Gao, D. (2015). Epithelial-to-mesenchymal transition is not required for lung metastasis but contributes to chemoresistance. *Nature*, *527*(7579), 472-476. https://doi.org/10.1038/nature15748

Friedl, P., & Gilmour, D. (2009). Collective cell migration in morphogenesis, regeneration and cancer [Review Article]. *Nature Reviews Molecular Cell Biology*, *10*, 445. https://doi.org/10.1038/nrm2720

Geudens, I., & Gerhardt, H. (2011). Coordinating cell behaviour during blood vessel formation. *Development*, *138*(21), 4569-4583. https://doi.org/10.1242/dev.062323

Gupton, S. L., & Waterman-Storer, C. M. (2006). Spatiotemporal feedback between actomyosin and focal-adhesion systems optimizes rapid cell migration. *Cell*, *125*(7), 1361-1374. https://doi.org/10.1016/j.cell.2006.05.029

Guy, C. T., Cardiff, R. D., & Muller, W. J. (1992). Induction of mammary tumors by expression of polyomavirus middle T oncogene: a transgenic mouse model for metastatic disease. *Mol Cell Biol*, *12*(3), 954-961. https://doi.org/10.1128/mcb.12.3.954

Habas, R., Dawid, I. B., & He, X. (2003). Coactivation of Rac and Rho by Wnt/Frizzled signaling is required for vertebrate gastrulation. *Genes Dev*, *17*(2), 295-309. https://doi.org/10.1101/gad.1022203

Habas, R., Kato, Y., & He, X. (2001). Wnt/Frizzled activation of Rho regulates vertebrate gastrulation and requires a novel Formin homology protein Daam1. *Cell*, *107*(7), 843-854. https://doi.org/10.1016/s0092-8674(01)00614-6

Hatakeyama, J., Wald, J. H., Printsev, I., Ho, H. Y., & Carraway, K. L., 3rd. (2014). Vangl1 and Vangl2: planar cell polarity components with a developing role in cancer. *Endocr Relat Cancer*, *21*(5), R345-356. https://doi.org/10.1530/ERC-14-0141

Hou, J. M., Krebs, M. G., Lancashire, L., Sloane, R., Backen, A., Swain, R. K., Priest, L. J., Greystoke, A., Zhou, C., Morris, K., Ward, T., Blackhall, F. H., & Dive, C. (2012). Clinical significance and molecular characteristics of circulating tumor cells and circulating tumor microemboli in patients with small-cell lung cancer. *J Clin Oncol*, *30*(5), 525-532. https://doi.org/10.1200/JCO.2010.33.3716

Itoh, R. E., Kurokawa, K., Ohba, Y., Yoshizaki, H., Mochizuki, N., & Matsuda, M. (2002). Activation of rac and cdc42 video imaged by fluorescent resonance energy transfer-based single-molecule probes in the membrane of living cells. *Mol Cell Biol*, *22*(18), 6582-6591. https://doi.org/10.1128/mcb.22.18.6582-6591.2002

Jenny, A., Reynolds-Kenneally, J., Das, G., Burnett, M., & Mlodzik, M. (2005). Diego and Prickle regulate Frizzled planar cell polarity signalling by competing for Dishevelled binding. *Nat Cell Biol*, *7*(7), 691-697. https://doi.org/10.1038/ncb1271

Karlsson, R., Pedersen, E. D., Wang, Z., & Brakebusch, C. (2009). Rho GTPase function in tumorigenesis. *Biochim Biophys Acta*, *1796*(2), 91-98. https://doi.org/10.1016/j.bbcan.2009.03.003

Kurayoshi, M., Oue, N., Yamamoto, H., Kishida, M., Inoue, A., Asahara, T., Yasui, W., & Kikuchi, A. (2006). Expression of Wnt-5a is correlated with aggressiveness of gastric cancer by stimulating cell migration and invasion. *Cancer Res*, *66*(21), 10439-10448. https://doi.org/10.1158/0008-5472.CAN-06-2359

Lin, E. Y., Jones, J. G., Li, P., Zhu, L., Whitney, K. D., Muller, W. J., & Pollard, J. W. (2003). Progression to malignancy in the polyoma middle T oncoprotein mouse breast cancer model provides a reliable model for human diseases. *Am J Pathol*, *163*(5), 2113-2126. https://doi.org/10.1016/S0002-9440(10)63568-7

Luga, V., Zhang, L., Viloria-Petit, A. M., Ogunjimi, A. A., Inanlou, M. R., Chiu, E., Buchanan, M., Hosein, A. N., Basik, M., & Wrana, J. L. (2012). Exosomes mediate stromal mobilization of autocrine Wnt-PCP signaling in breast cancer cell migration. *Cell*, *151*(7), 1542-1556. https://doi.org/10.1016/j.cell.2012.11.024

MacMillan, C. D., Leong, H. S., Dales, D. W., Robertson, A. E., Lewis, J. D., Chambers, A. F., & Tuck, A. B. (2014). Stage of breast cancer progression influences cellular response to activation of the WNT/planar cell polarity pathway. *Sci Rep*, *4*, 6315. https://doi.org/10.1038/srep06315

Mayor, R., & Etienne-Manneville, S. (2016). The front and rear of collective cell migration. *Nat Rev Mol Cell Biol*, *17*(2), 97-109. https://doi.org/10.1038/nrm.2015.14

Miller, J. K., Shattuck, D. L., Ingalla, E. Q., Yen, L., Borowsky, A. D., Young, L. J., Cardiff, R. D., Carraway, K. L., 3rd, & Sweeney, C. (2008). Suppression of the negative regulator LRIG1 contributes to ErbB2 overexpression in breast cancer. *Cancer Res*, *68*(20), 8286-8294. https://doi.org/10.1158/0008-5472.CAN-07-6316

Minegishi, K., Hashimoto, M., Ajima, R., Takaoka, K., Shinohara, K., Ikawa, Y., Nishimura, H., McMahon, A. P., Willert, K., Okada, Y., Sasaki, H., Shi, D., Fujimori, T., Ohtsuka, T., Igarashi, Y., Yamaguchi, T. P., Shimono, A., Shiratori, H., & Hamada, H. (2017). A Wnt5 Activity Asymmetry and Intercellular Signaling via PCP Proteins Polarize Node Cells for Left-Right Symmetry Breaking. *Dev Cell*, *40*(5), 439-452 e434. https://doi.org/10.1016/j.devcel.2017.02.010

Murdoch, J. N., Doudney, K., Paternotte, C., Copp, A. J., & Stanier, P. (2001). Severe neural tube defects in the loop-tail mouse result from mutation of Lpp1, a novel gene involved in floor plate specification. *Hum Mol Genet*, *10*(22), 2593-2601. https://doi.org/10.1093/hmg/10.22.2593

Nguyen-Ngoc, K. V., Cheung, K. J., Brenot, A., Shamir, E. R., Gray, R. S., Hines, W. C., Yaswen, P., Werb, Z., & Ewald, A. J. (2012). ECM microenvironment regulates collective migration and local

dissemination in normal and malignant mammary epithelium. *Proc Natl Acad Sci U S A*, *109*(39), E2595-2604. https://doi.org/10.1073/pnas.1212834109

Nishioka, M., Ueno, K., Hazama, S., Okada, T., Sakai, K., Suehiro, Y., Okayama, N., Hirata, H., Oka, M., Imai, K., Dahiya, R., & Hinoda, Y. (2013). Possible involvement of Wnt11 in colorectal cancer progression. *Mol Carcinog*, *52*(3), 207-217. https://doi.org/10.1002/mc.21845

Otsu, N. (1979). A Threshold Selection Method for Gray-Level Histograms. *Transactions on Systems, Man, and Cybernetics*, *SMC-9*(1), 62-66.

Proffitt, K. D., Madan, B., Ke, Z., Pendharkar, V., Ding, L., Lee, M. A., Hannoush, R. N., & Virshup, D. M. (2013). Pharmacological inhibition of the Wnt acyltransferase PORCN prevents growth of WNT-driven mammary cancer. *Cancer Res*, *73*(2), 502-507. https://doi.org/10.1158/0008-5472.CAN-12-2258

Pukrop, T., Klemm, F., Hagemann, T., Gradl, D., Schulz, M., Siemes, S., Trumper, L., & Binder, C. (2006). Wnt 5a signaling is critical for macrophage-induced invasion of breast cancer cell lines. *Proc Natl Acad Sci U S A*, *103*(14), 5454-5459. https://doi.org/10.1073/pnas.0509703103

Puvirajesinghe, T. M., Bertucci, F., Jain, A., Scerbo, P., Belotti, E., Audebert, S., Sebbagh, M., Lopez, M., Brech, A., Finetti, P., Charafe-Jauffret, E., Chaffanet, M., Castellano, R., Restouin, A., Marchetto, S., Collette, Y., Goncalves, A., Macara, I., Birnbaum, D., Kodjabachian, L., Johansen, T., & Borg, J. P. (2016). Identification of p62/SQSTM1 as a component of non-canonical Wnt VANGL2-JNK signalling in breast cancer. *Nat Commun*, *7*, 10318. https://doi.org/10.1038/ncomms10318

Reffay, M., Parrini, M. C., Cochet-Escartin, O., Ladoux, B., Buguin, A., Coscoy, S., Amblard, F., Camonis, J., & Silberzan, P. (2014). Interplay of RhoA and mechanical forces in collective cell migration driven by leader cells. *Nat Cell Biol*, *16*(3), 217-223. https://doi.org/10.1038/ncb2917

Ridley, A. J. (2015). Rho GTPase signalling in cell migration. *Curr Opin Cell Biol*, *36*, 103-112. https://doi.org/10.1016/j.ceb.2015.08.005

Rowson-Hodel, A. R., Manjarin, R., Trott, J. F., Cardiff, R. D., Borowsky, A. D., & Hovey, R. C. (2015). Neoplastic transformation of porcine mammary epithelial cells in vitro and tumor formation in vivo. *BMC Cancer*, *15*, 562. https://doi.org/10.1186/s12885-015-1572-7

Rowson-Hodel, A. R., Wald, J. H., Hatakeyama, J., O'Neal, W. K., Stonebraker, J. R., VanderVorst, K., Saldana, M. J., Borowsky, A. D., Sweeney, C., & Carraway, K. L., 3rd. (2018). Membrane Mucin Muc4 promotes blood cell association with tumor cells and mediates efficient metastasis in a mouse model of breast cancer. *Oncogene*, *37*(2), 197-207. https://doi.org/10.1038/onc.2017.327

Semenov, M. V., Habas, R., Macdonald, B. T., & He, X. (2007). SnapShot: Noncanonical Wnt Signaling Pathways. *Cell*, *131*(7), 1378. https://doi.org/10.1016/j.cell.2007.12.011

Siegel, P. M., Ryan, E. D., Cardiff, R. D., & Muller, W. J. (1999). Elevated expression of activated forms of Neu/ErbB-2 and ErbB-3 are involved in the induction of mammary tumors in transgenic mice: implications for human breast cancer. *EMBO J*, *18*(8), 2149-2164. https://doi.org/10.1093/emboj/18.8.2149

Steeg, P. S. (2016). Targeting metastasis. *Nat Rev Cancer*, *16*(4), 201-218. https://doi.org/10.1038/nrc.2016.25

Strutt, H., & Strutt, D. (2008). Differential stability of flamingo protein complexes underlies the establishment of planar polarity. *Curr Biol*, *18*(20), 1555-1564. https://doi.org/10.1016/j.cub.2008.08.063

Talmadge, J. E., & Fidler, I. J. (2010). AACR centennial series: the biology of cancer metastasis: historical perspective. *Cancer Res*, *70*(14), 5649-5669. https://doi.org/10.1158/0008-5472.CAN-10-1040

Tree, D. R., Shulman, J. M., Rousset, R., Scott, M. P., Gubb, D., & Axelrod, J. D. (2002). Prickle mediates feedback amplification to generate asymmetric planar cell polarity signaling. *Cell*, *109*(3), 371-381. https://www.ncbi.nlm.nih.gov/pubmed/12015986

964 Ueno, K., Hiura, M., Suehiro, Y., Hazama, S., Hirata, H., Oka, M., Imai, K., Dahiya, R., & Hinoda, Y. (2008).
965 Frizzled-7 as a potential therapeutic target in colorectal cancer. *Neoplasia*, *10*(7), 697-705.
966 https://www.ncbi.nlm.nih.gov/pubmed/18592008
967 Uphoff, C. C., & Drexler, H. G. (2002). Comparative PCR analysis for detection of mycoplasma infections
968 in continuous cell lines. *In Vitro Cell Dev Biol Anim*, *38*(2), 79-85. https://doi.org/10.1290/1071-
969 2690(2002)038<0079:CPAFDO>2.0.CO;2
970 Uphoff, C. C., & Drexler, H. G. (2004). Detecting Mycoplasma contamination in cell cultures by
971 polymerase chain reaction. *Methods Mol Med*, *88*, 319-326. https://doi.org/10.1385/1-59259-
972 406-9:319
973 Uysal-Onganer, P., Kawano, Y., Caro, M., Walker, M. M., Diez, S., Darrington, R. S., Waxman, J., & Kypta,
974 R. M. (2010). Wnt-11 promotes neuroendocrine-like differentiation, survival and migration of
975 prostate cancer cells. *Mol Cancer*, *9*, 55. https://doi.org/10.1186/1476-4598-9-55
976 van Amerongen, R. (2012). Alternative Wnt pathways and receptors. *Cold Spring Harb Perspect Biol*,
977 *4*(10). https://doi.org/10.1101/cshperspect.a007914
978 VanderVorst, K., Dreyer, C. A., Konopelski, S. E., Lee, H., Ho, H. H., & Carraway, K. L., 3rd. (2019).
979 Wnt/PCP Signaling Contribution to Carcinoma Collective Cell Migration and Metastasis. *Cancer*
980 *Res*, *79*(8), 1719-1729. https://doi.org/10.1158/0008-5472.CAN-18-2757
981 VanderVorst, K., Hatakeyama, J., Berg, A., Lee, H., & Carraway, K. L., 3rd. (2018). Cellular and molecular
982 mechanisms underlying planar cell polarity pathway contributions to cancer malignancy. *Semin*
983 *Cell Dev Biol*, *81*, 78-87. https://doi.org/10.1016/j.semcdb.2017.09.026
984 Wagner, K. U., Wall, R. J., St-Onge, L., Gruss, P., Wynshaw-Boris, A., Garrett, L., Li, M., Furth, P. A., &
985 Hennighausen, L. (1997). Cre-mediated gene deletion in the mammary gland. *Nucleic Acids Res*,
986 *25*(21), 4323-4330. https://doi.org/10.1093/nar/25.21.4323
987 Wald, J. H., Hatakeyama, J., Printsev, I., Cuevas, A., Fry, W. H. D., Saldana, M. J., VanderVorst, K.,
988 Rowson-Hodel, A., Angelastro, J. M., Sweeney, C., & Carraway Rd, K. L. (2017). Suppression of
989 planar cell polarity signaling and migration in glioblastoma by Nrdp1-mediated Dvl
990 polyubiquitination. *Oncogene*. https://doi.org/10.1038/onc.2017.126
991 Warrington, S. J., Strutt, H., Fisher, K. H., & Strutt, D. (2017). A Dual Function for Prickle in Regulating
992 Frizzled Stability during Feedback-Dependent Amplification of Planar Polarity. *Curr Biol*, *27*(18),
993 2784-2797 e2783. https://doi.org/10.1016/j.cub.2017.08.016
994 Wu, J., & Mlodzik, M. (2008). The frizzled extracellular domain is a ligand for Van Gogh/Stbm during
995 nonautonomous planar cell polarity signaling. *Dev Cell*, *15*(3), 462-469.
996 https://doi.org/10.1016/j.devcel.2008.08.004
997 Wu, J., Roman, A. C., Carvajal-Gonzalez, J. M., & Mlodzik, M. (2013). Wg and Wnt4 provide long-range
998 directional input to planar cell polarity orientation in Drosophila. *Nat Cell Biol*, *15*(9), 1045-1055.
999 https://doi.org/10.1038/ncb2806
1000 Yang, H. W., Collins, S. R., & Meyer, T. (2016). Locally excitable Cdc42 signals steer cells during
1001 chemotaxis. *Nat Cell Biol*, *18*(2), 191-201. https://doi.org/10.1038/ncb3292
1002 Ybot-Gonzalez, P., Savery, D., Gerrelli, D., Signore, M., Mitchell, C. E., Faux, C. H., Greene, N. D., & Copp,
1003 A. J. (2007). Convergent extension, planar-cell-polarity signalling and initiation of mouse neural
1004 tube closure. *Development*, *134*(4), 789-799. https://doi.org/10.1242/dev.000380
1005 Zegers, M. M., & Friedl, P. (2014). Rho GTPases in collective cell migration. *Small GTPases*, *5*, e28997.
1006 https://doi.org/10.4161/sgtp.28997
1007 Zhang, L., Luga, V., Armitage, S. K., Musiol, M., Won, A., Yip, C. M., Plotnikov, S. V., & Wrana, J. L. (2016).
1008 A lateral signalling pathway coordinates shape volatility during cell migration. *Nat Commun*, *7*,
1009 11714. https://doi.org/10.1038/ncomms11714
1010
1011

1012 **SUPPLEMENTARY FIGURES and LEGENDS**

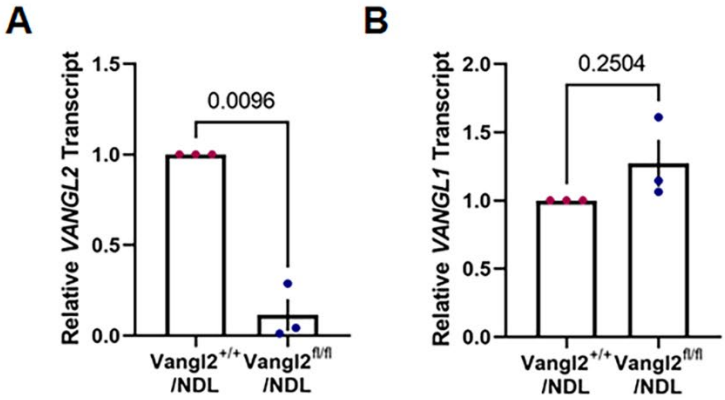

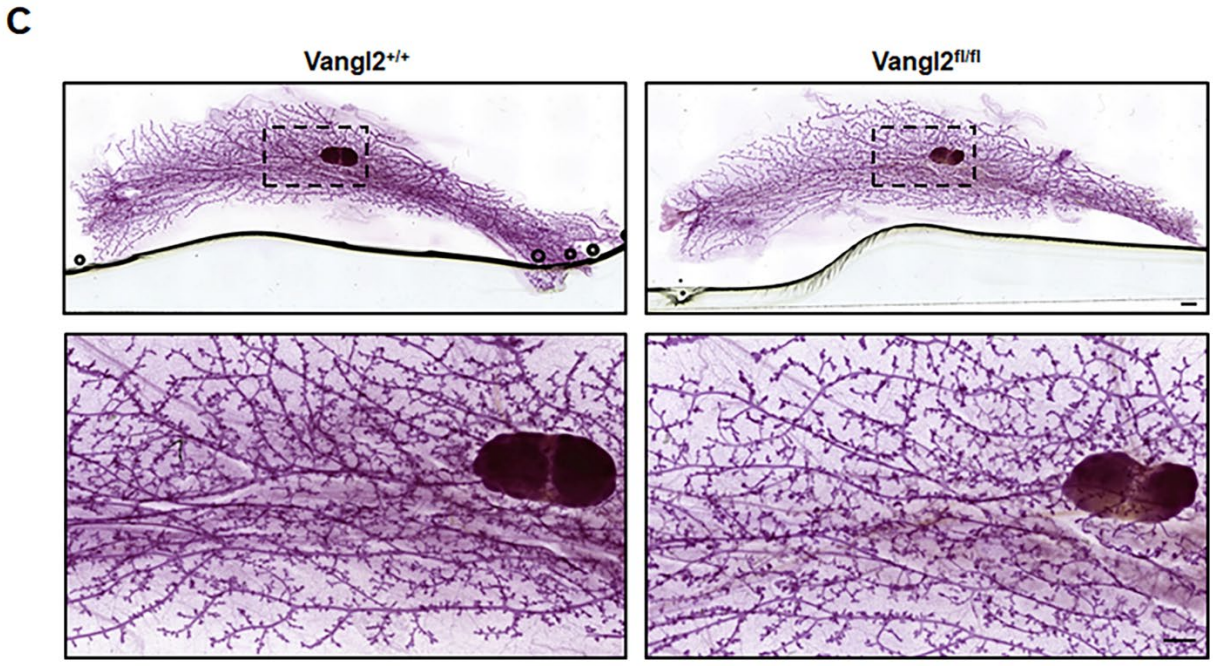

1014

Figure 1–figure supplement 1. Functional Vangl2 deletion is evident by transcript. a-b *VANGL2* **(A)** and *VANGL1* **(B)** transcript from Vangl2$^{fl/fl}$/NDL and Vangl2$^{+/+}$/NDL primary tumors by *q*PCR from three tumors of independent biological sources per genotype. **c** Carmine alum stained mammary whole mounts from estrus matched 20-week-old Vangl2$^{+/+}$ and Vangl2$^{fl/fl}$ mice, demonstrating no detectable differences in gland architecture in adult virgin mice. Scale bars = 1mm (top panels) or 500μm (bottom panels).

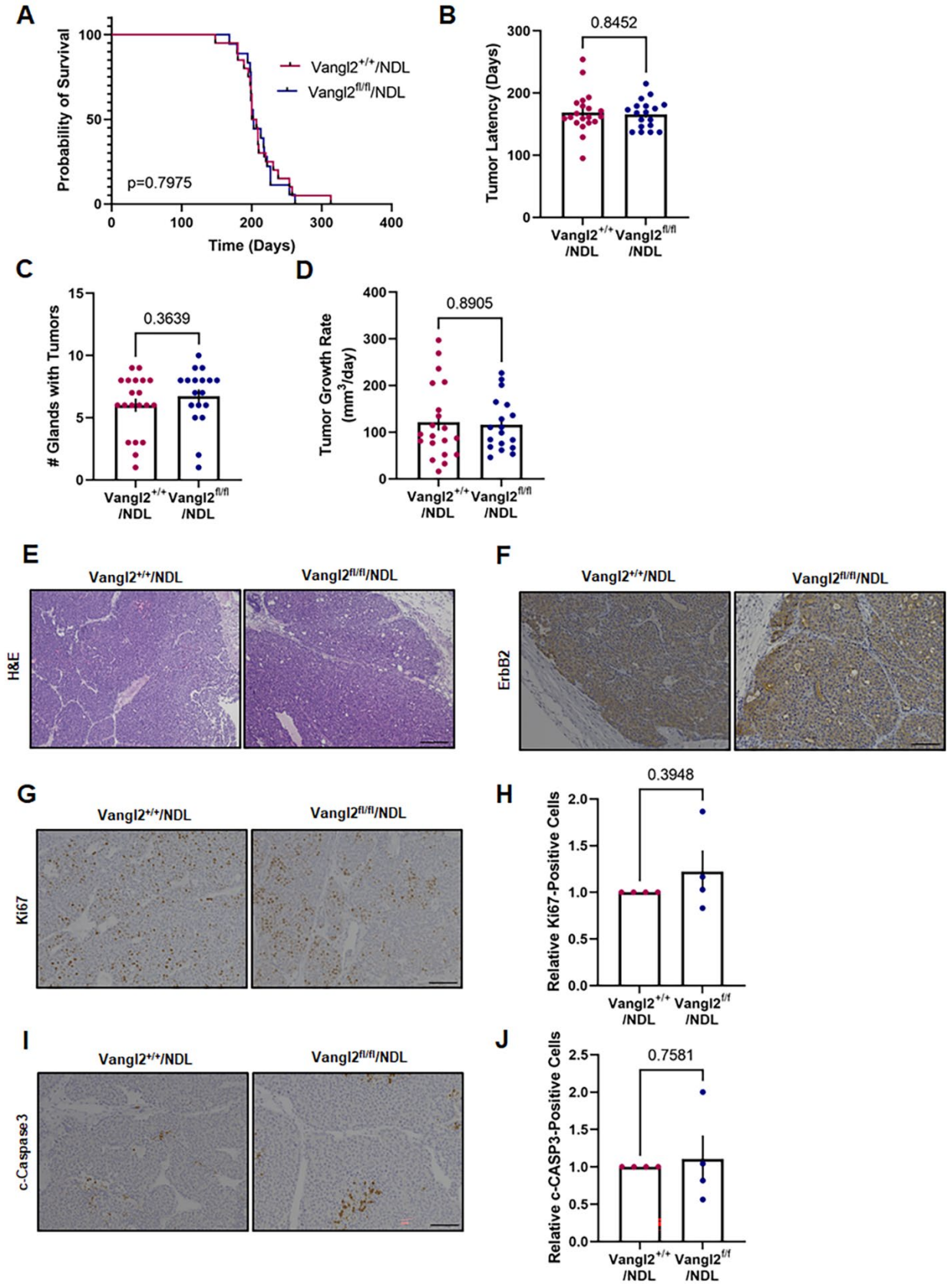

1022

Figure 1–figure supplement 2. Vangl2 deletion does not impact primary tumor growth characteristics or histology. A-D Survival curves and bar graphs depicting Vangl2/NDL tumor initiation and growth characteristics. Probability of survival **(A),** tumor latency **(B),** number of glands with tumors **(C),** and tumor growth rate **(D)** for Vangl2$^{+/+}$/NDL (*n*=20) and Vangl2$^{fl/fl}$/NDL (*n*=20) tumor-bearing animals. **E,F** Representative images are depicted of formalin fixed, paraffin embedded sections from Vangl2$^{+/+}$/NDL and Vangl2$^{fl/fl}$/NDL primary tumors stained with H&E **(E)** or following immunodetection with ErbB2 **(F)**, scale bar=200μm. **G-J** Representative images of Vangl2$^{+/+}$/NDL and Vangl2$^{fl/fl}$/NDL primary tumor tissues following immunodetection of proliferation marker Ki67 **(G)** with quantification of Ki67-positive cells (*n*=4) **(H)** and apoptosis marker cleaved caspase-3 **(I)** with quantification of c-Caspase 3-positive cells (*n*=4) **(J)**, scale bar=100μm. Significance determined by Log-rank **(A)** or Mann-Whitney test **(C,D)** or two-sided unpaired *t*-test with Welch's correction **(H,J)**. All bar graphs represent the mean ± sem of experimental replicates (*n*).

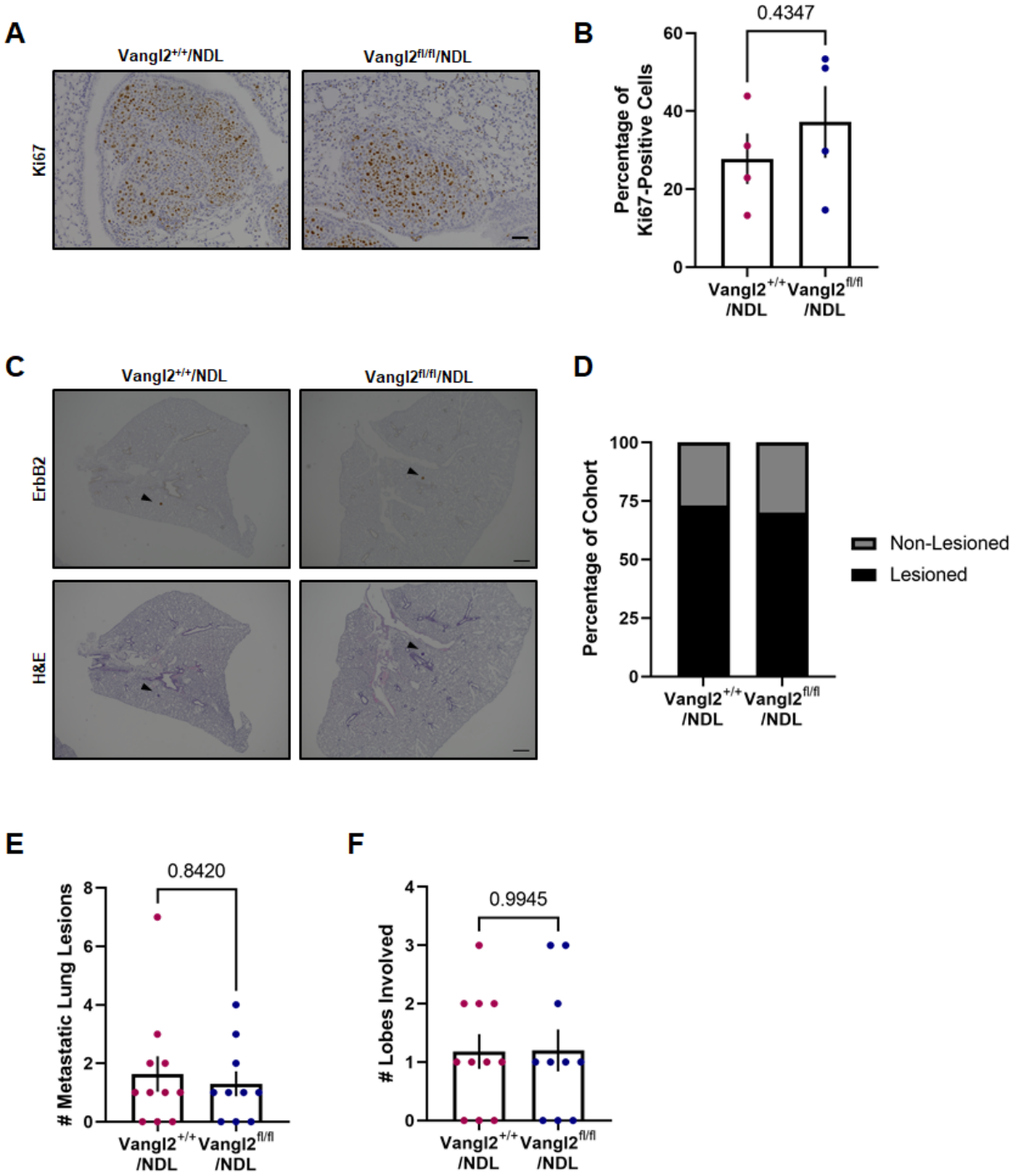

1038

Figure 1–figure supplement 3. Vangl2 is dispensable for metastatic lesion colonization and proliferation. A,B Metastatic lung lesions of Vangl2$^{+/+}$/NDL (*n*=4) and Vangl2$^{fl/fl}$/NDL tumor-bearing mice (*n*=4) were evaluated for proliferative capacity by immunodetection of Ki67 **(A)** and the percentage of Ki67-positive cells was quantified **(B). C** Representative images of formalin fixed, paraffin embedded sections of lungs from FvB/NJ mice receiving Vangl2$^{+/+}$/NDL or Vangl2$^{fl/fl}$/NDL cells via the tail vein following immunodetection of ErbB2 (top panel) and H&E staining (bottom panel). Examples of ErbB2-positive metastatic lung lesions are denoted by black arrowheads, scale bar =500μm. **D-F** Lung lobes (5 lobes per mouse) from FvB/NJ mice receiving Vangl2$^{+/+}$/NDL or Vangl2$^{fl/fl}$/NDL cells via the tail vein were evaluated by histology for the occurrence of metastatic lesions for Vangl2$^{+/+}$/NDL (*n*=11) and Vangl2$^{fl/fl}$/NDL (*n*=10) cohorts. The number of mice bearing metastatic lesions **(D)**, numbers of metastatic lesions **(E)**, and numbers of lung lobes involved **(F)** were assessed. Significance was determined by Mann-Whitney test and bar graphs represent the mean ± sem of experimental replicates (*n*).

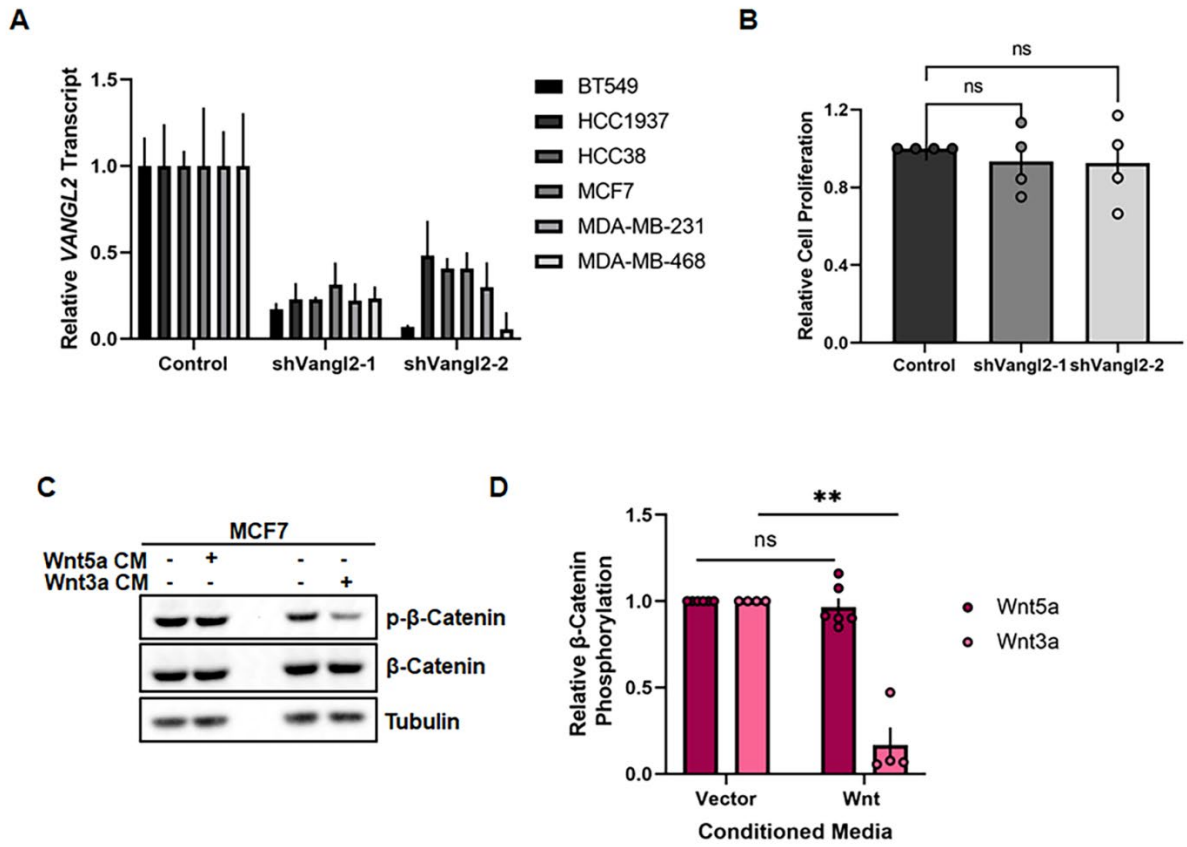

1054 **Figure 2–figure supplement 1. Supporting materials for Figure 2. A** Relative *VANGL2*
1055 transcript in BT549, HCC1937, HCC38, MCF7, MDA-MB-231, and MDA-MB-468 stably
1056 expressing Control, shVangl2-1, or shVangl2-2 by *q*-PCR. **B** Quantification of relative cell
1057 proliferation of MCF7 cells stably expressing Control, shVangl2-1, or shVangl2-2 (*n*=4). **C,D**
1058 MCF7 cells stimulated with Vector- or Wnt5a-conditioned media or Vector- or Wnt3a-conditioned
1059 media for 1 hour blotted for β-Catenin and phospho-β-Catenin (Ser33/37/Thr41) **(C)** and
1060 quantification of relative phosho-β-Catenin (Ser33/37/Thr41) (control- vs Wnt5a-conditioned
1061 media *n*=6, *p*=0.5419, control- vs Wnt3a-conditioned media *n*=4, *p*=0.0038) **(D)**. Bar graphs
1062 represent the mean ± sem of experimental replicates (*n*). Significance was determined by a two-
1063 sided unpaired *t*-test with Welch's correction, **p* < 0.05, ***p* < 0.01, ****p* < 0.001, *****p* < 0.0001.

1064

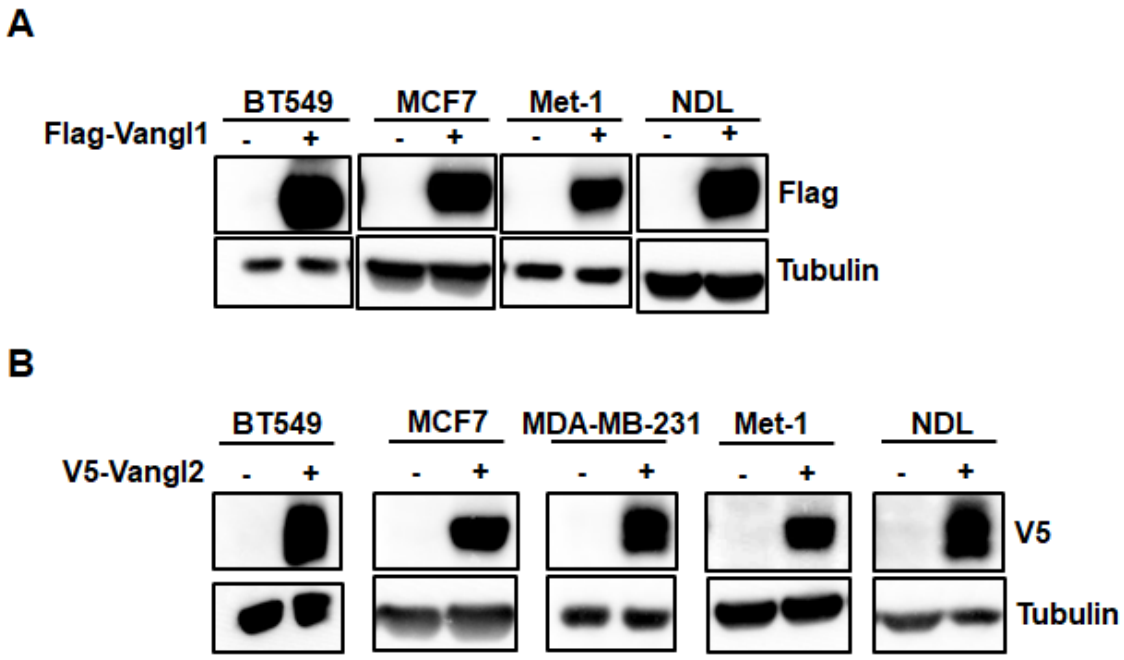

Figure 3–figure supplement 1. Overexpression of Wnt/PCP components. A,B Breast cancer cell lines stably overexpressing Flag-Vangl1 blotted for Flag **(A)** or V5-Vangl2 blotted for V5 **(B).**

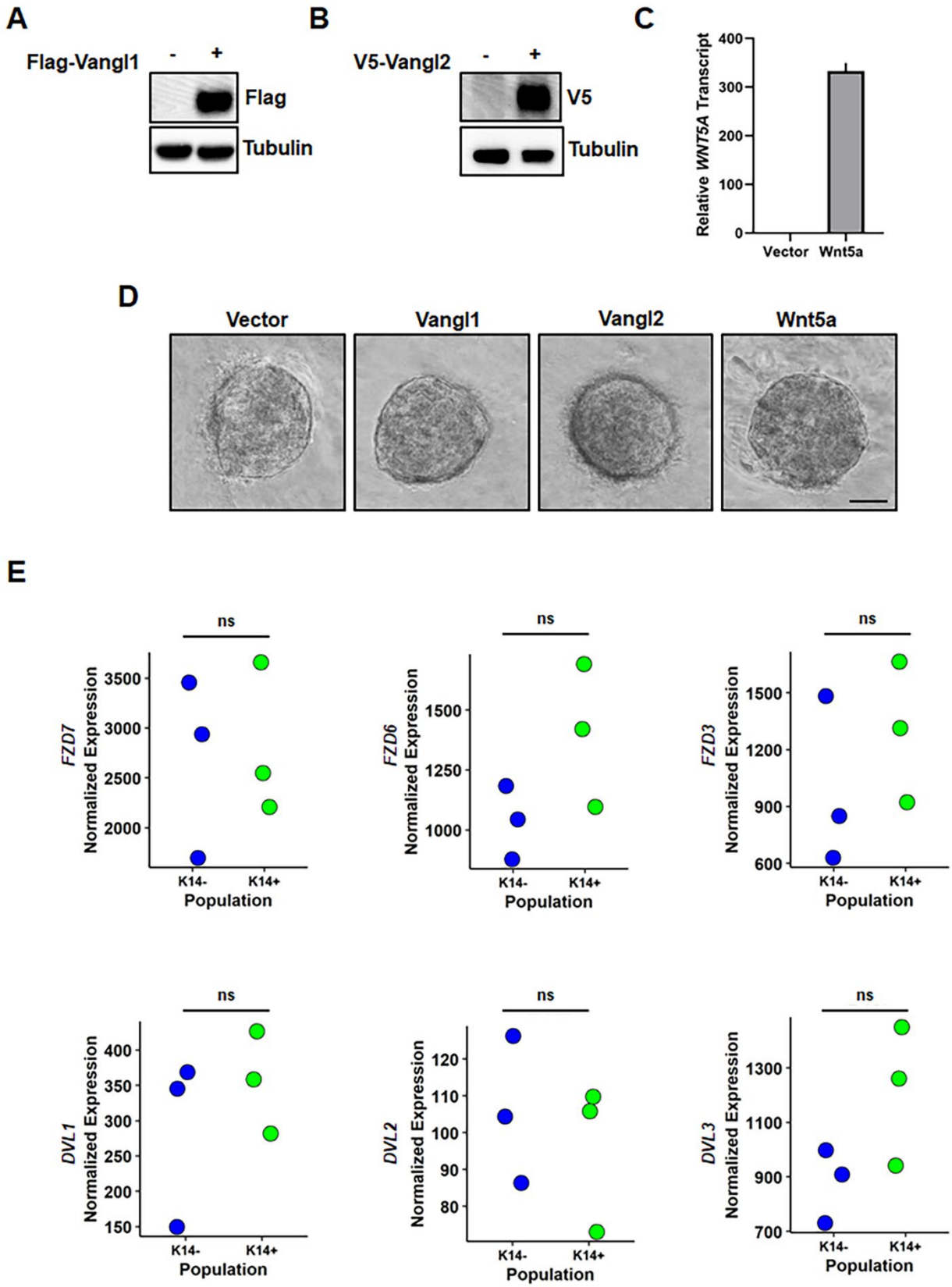

Figure 4–figure supplement 1. Supporting materials for Figure 4. A-C *MMTV-PyMT*-derived tumor organoid cells stably overexpressing Vangl1, Vangl2, or Wnt5a were assessed for Flag-Vangl1 **(A)** or V5-Vangl2 **(B)** expression by Western blot or *WNT5A* transcript by qPCR **(C)**. **D** Representative images of Vector-, Vangl1-, Vangl2-, and Wnt5a-expressing *MMTV-PyMT*-derived tumor organoids in collagen in the absence of *b*FGF, scale bar=50µm. **E** Analysis of RNA-sequencing data set SRP066316 from NCBI Sequence Read Archive for *Fzd7*, *Fzd6, Fzd3, Dvl1, Dvl2*, and *Dvl3* transcript in K14-negative and K14-postive cells derived from *MMTV-PyMT* tumors.

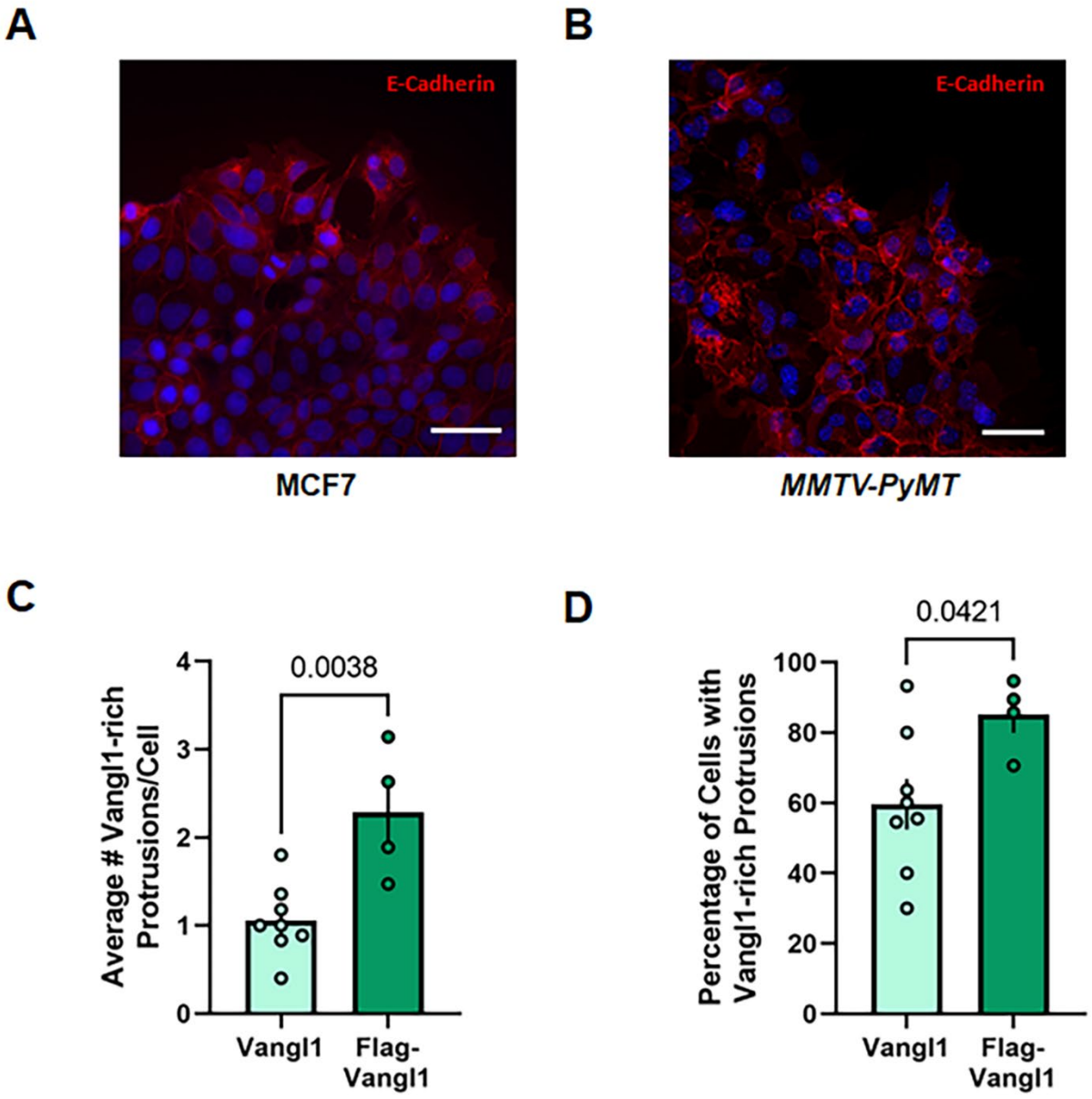

Figure 5–figure supplement 1. Supporting materials for Figure 5. A,B Representative confocal images of collectively migrating MCF7 **(A)** and MMTV-PyMT tumor-derived **(B)** cells stained for E-Cadherin: orange and DAPI: blue, scale bar = 50μm. **C** Quantification of the average number of Vangl1-rich protrusions per leading-edge cell in collectively migrating MCF7-Vector and MCF7-Flag-Vangl1 cells (MCF7-Vector *n*=8 *scratches quantified,* MCF7-Flag-Vangl1 *n*=4 *scratches quantified*, *p*=0.0038) **D** Quantification of the percentage of leading-edge cells with Vangl1-rich protrusions (MCF7-Vector *n*=8, MCF7-Flag-Vangl1 *n*=4, *p*=0.0421). Bar graphs represent the mean ± sem of experimental replicates (*n*). Significance was determined by a two-sided unpaired *t*-test with Welch's correction.

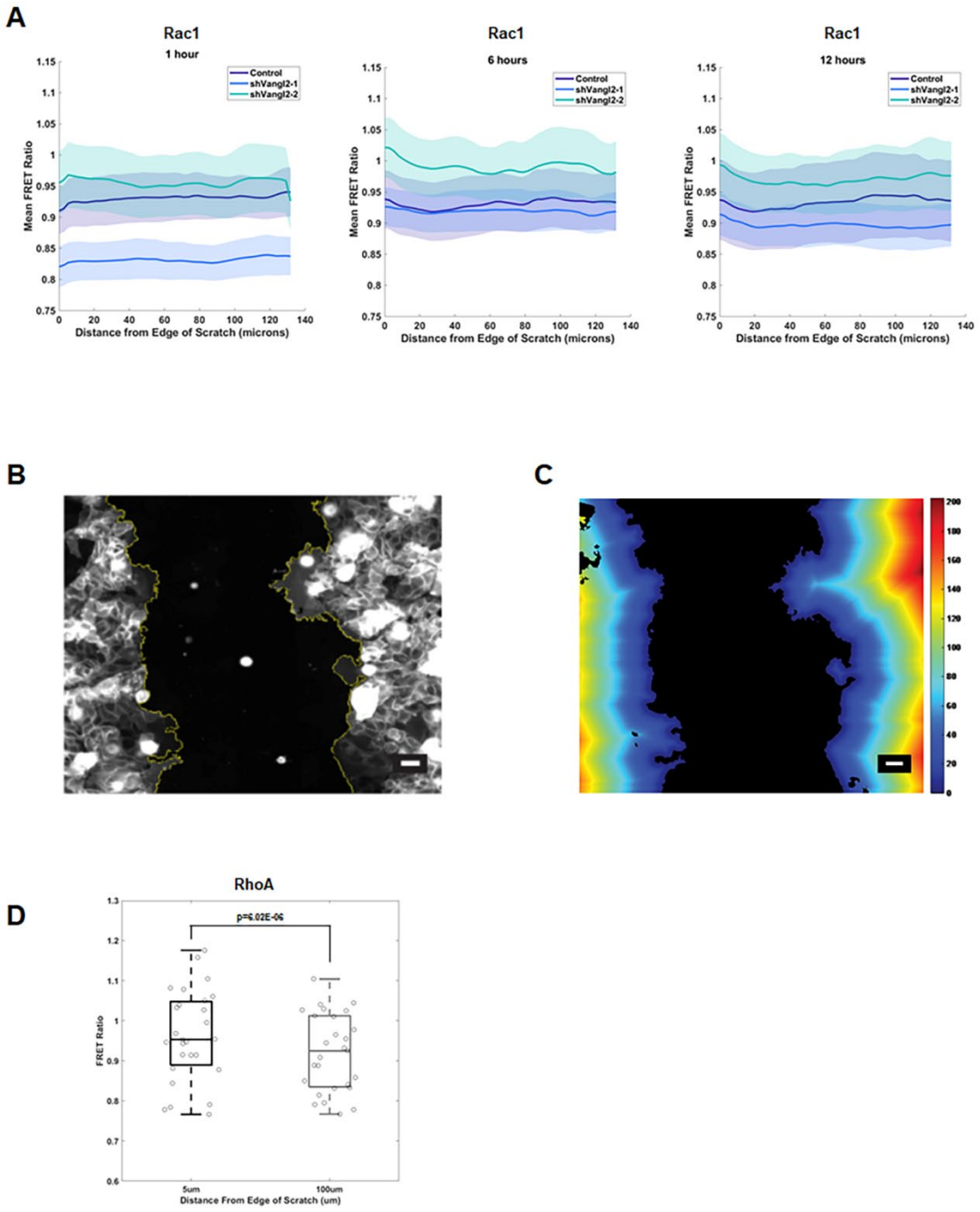

Figure 6–figure supplement 1. Supporting materials for Figure 6. A Rac1 activity as a function of distance in microns from the leading-edge of collectively migrating MCF7 cells stably expressing Vector (*n*=27 wells), shVangl2-1 (*n*=24 wells), or shVangl2-2 (*n*=25 wells) at 1, 6, and 12 hours of migration, error bars indicate ± sem. **B,C** Representative example of custom MATLAB script identifying the leading-edge of a migrating cohort of MCF7 cells **(B)** and binned migrating cells based on their distance from the edge of the scratch in microns, where color bar indicates the distance from the leading-edge of the scratch **(C)**, scale bars=25μm. **D** RhoA activity in MCF7 cells stably expressing the RhoA biosensor and Control at 5μm and 100μm from the edge the of scratch (*n*=27, *p*=6.02E-06), significance was determined by a two-sided paired *t*-test.

Supplementary Video 1. RhoA-FRET biosensor video of MCF7-Control. Representative videos of spatial activity profiles of RhoA in collectively migrating MCF7 cells stably expressing RhoA-FRET biosensor for Control over 12 hours. Color bars indicate the range of RhoA-FRET biosensor ratios. Scale bar=25μm.

Supplementary Video 2. RhoA-FRET biosensor video of MCF7-shVangl2-1. Representative videos of spatial activity profiles of RhoA in collectively migrating MCF7 cells stably expressing RhoA-FRET biosensor for shVangl2-1 over 12 hours. Color bars indicate the range of RhoA-FRET biosensor ratios. Scale bar=25μm.

Supplementary Video 3. RhoA-FRET biosensor video of MCF7-shVangl2-2. Representative videos of spatial activity profiles of RhoA in collectively migrating MCF7 cells stably expressing RhoA-FRET biosensor for shVangl2-2 over 12 hours. Color bars indicate the range of RhoA-FRET biosensor ratios. Scale bar=25μm.

Immunoblot Source Files. The raw data corresponding to Figures 2D, 3E and 3G, and Figure 2-figure supplement 1C, Figure 3-figure supplements 1A and 1B, and Figure 4-figure supplements 1A and 1B, are compiled in eight folders. Regions of blots included in figures are indicated by red boxes in two Word documents.